

ERRATA - JUNE 1995

THE FOLLOWING CORRECTION IS APPLICABLE TO WL-TR-95-3044, ENTITLED  
"A COMPUTATIONAL MODEL FOR PROGRESSIVE DAMAGE AND FAILURE OF  
FIBER-REINFORCED CERAMIC COMPOSITES," DATED FEBRUARY 1995:

COVER PAGE

INSERT THE LAST WORD OF THE TITLE TO READ: ...COMPOSITES

FLIGHT DYNAMICS DIRECTORATE  
WRIGHT LABORATORY  
AIR FORCE MATERIEL COMMAND  
WRIGHT PATTERSON AFB OH 45433-7562

WL-TR-95-3044

A COMPUTATIONAL MODEL FOR PROGRESSIVE DAMAGE  
AND FAILURE OF FIBER-REINFORCED CERAMIC  
COMPOSITES



LUEN-YUAN CHAO AND DINESH K SHETTY

MATERIALS AND SYSTEMS RESEARCH, INC  
62 EAST CLEVELAND AVE  
SALT LAKE CITY, UT 84115

FEBRUARY 1995

FINAL REPORT FOR 07/12/94-01/12/95

APPROVED FOR PUBLIC RELEASE; DISTRIBUTION IS UNLIMITED.

FLIGHT DYNAMICS DIRECTORATE  
WRIGHT LABORATORY  
AIR FORCE MATERIEL COMMAND  
WRIGHT PATTERSON AFB OH 45433-7562

1995 0619 042

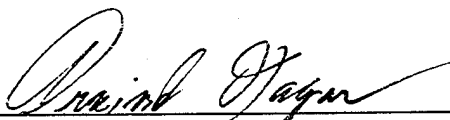
~~19950629 011~~

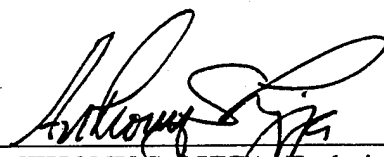
## NOTICE


When Government drawings, specifications, or other data are used for any purpose other than in connection with a definitely Government-related procurement, the United States Government incurs no responsibility or any obligation whatsoever. The fact that the government may have formulated or in any way supplied the said drawings, specifications, or other data, is not to be regarded by implication, or otherwise in any manner construed, as licensing the holder, or any other person or corporation; or as conveying any rights or permission to manufacture, use, or sell any patented invention that may in any way be related thereto.

This report is releasable to the National Technical Information Service (NTIS). At NTIS, it will be available to the general public, including foreign nations.

This technical report has been reviewed and is approved for publication.

  
ARVIND NAGAR, Aero Engr  
Fatigue, Fracture & Reliability Section

  
ANTHONY S. LIZZA, Technical Mgr  
Fatigue, Fracture & Reliability Section

  
JEROME PEARSON, Chief  
Structural Integrity Branch  
Structures Division

If your address has changed, if you wish to be removed from our mailing list, or if the addressee is no longer employed by your organization, please notify WL/FIBEC, Building 45, 2130 Eighth Street, Suite 1, Wright-Patterson AFB, OH, 45433-7542 to help us maintain a current mailing list.

Copies of this report should not be returned unless return is required by security considerations, contractual obligations, or notice on a specific document.

REPORT DOCUMENTATION PAGE			Form Approved OMB No. 0704-0188	
Public reporting burden for this collection of information is estimated to average 1 hour per response, including the time for reviewing instructions, searching existing data sources, gathering and maintaining the data needed, and completing and reviewing the collection of information. Send comments regarding this burden estimate or any other aspect of this collection of information, including suggestions for reducing this burden, to Washington Headquarters Services, Directorate for Information Operations and Reports, 1215 Jefferson Davis Highway, Suite 1204, Arlington, VA 22202-4302, and to the Office of Management and Budget, Paperwork Reduction Project (0704-0188), Washington, DC 20503.				
1. AGENCY USE ONLY (Leave blank)	2. REPORT DATE Feb. 12, 1995	3. REPORT TYPE AND DATES COVERED Final, July 12, 1994 ~ Jan. 12, 1995		
4. TITLE AND SUBTITLE  A Computational Model For Progressive Damage and Failure of Fiber-Reinforced Ceramic Composites		5. FUNDING NUMBERS  C F33657-94-C-2220 PE 65502F PR 3005 TA 08 WU 01		
6. AUTHOR(S)  Luen-Yuan Chao and Dinesh K. Shetty				
7. PERFORMING ORGANIZATION NAME(S) AND ADDRESS(ES)  Materials and Systems Research, Inc. 62 East, Cleveland Ave. Salt Lake City, UT 84115		8. PERFORMING ORGANIZATION REPORT NUMBER  MSRI-AF-9501		
9. SPONSORING / MONITORING AGENCY NAME(S) AND ADDRESS(ES)  WL/FIBEC (Dr. Arvind Nagar) Wright Laboratory Wright-Patterson AFB, OH 45433		10. SPONSORING / MONITORING AGENCY REPORT NUMBER  WL-TR-95-3044		
11. SUPPLEMENTARY NOTES  This is a Small Business Innovation Research (SBIR) Phase 1 report.				
12a. DISTRIBUTION / AVAILABILITY STATEMENT  Approved for public release; distribution unlimited.		12b. DISTRIBUTION CODE		
13. ABSTRACT (Maximum 200 words)  A computational model was developed to simulate the progressive damage of fiber-reinforced brittle matrix composites under uniaxial tensile loading. In conjunction with the basic material properties, this model used a size-distribution of the 'fiber-free zones' as an input for the development of small penny-shaped cracks at the early stage of loading. Stable extension of such non-steady-state cracks and the transition from non-steady-state to steady-state cracks were modeled using a stress-intensity formulation for a partially-bridged penny-shaped crack. Stress-strain relation was simulated by calculating the total engineering strain in the gage section as a function of the applied stress. Strain energies of the non-steady-state cracks and displacements of the fibers in the sliding zones of the steady-state cracks were calculated to estimate the total strain. Two unidirectional fiber-reinforced composites were investigated to test the predictive capability of this model. The stress-strain relation predicted by the model was in good agreement with that measured experimentally for a SiC-reinforced calcium aluminosilicate composite. A SiC-reinforced magnesium aluminosilicate composite showed less cumulative strain before fracture due to premature fiber failure.				
14. SUBJECT TERMS  Fiber-Reinforced Ceramic Composites, Fiber-Free Zones, Matrix Cracking, Modeling, Stress-Strain Relation.			15. NUMBER OF PAGES 54	
			16. PRICE CODE	
17. SECURITY CLASSIFICATION OF REPORT UNCLASSIFIED	18. SECURITY CLASSIFICATION OF THIS PAGE UNCLASSIFIED	19. SECURITY CLASSIFICATION OF ABSTRACT UNCLASSIFIED	20. LIMITATION OF ABSTRACT UL	

## TABLE OF CONTENTS

	Page
1. INTRODUCTION AND SUMMARY.....	1
1.1 Introduction .....	1
1.2 Summary.....	3
2. TECHNICAL BACKGROUND.....	4
2.1 Critical Stress for Extension of Steady-State Matrix Crack.....	4
2.2 Critical Stress for Extension of Short Cracks.....	5
2.3 Fracture Criterion.....	7
3. RESEARCH OBJECTIVES.....	9
4. TECHNICAL APPROACH OF THE MODEL.....	10
4.1 Model of Crack Evolution .....	10
4.2 Materials Properties.....	10
4.3 Characterization of the Microstructure and Fiber-Free Zones (FFZs).....	12
4.4 Distribution of FFZs in the Gage Section of the Composite.....	15
4.5 Transformation of FFZs to Cracks and Cracking Stress-Crack Size Relation.....	16
4.6 Simulation of the Stress-Strain Relation.....	19
5. EXPERIMENTAL PROCEDURE.....	23
5.1 Specimen Preparation.....	23
5.2 Edge-Loading Tensile Test.....	23
6. RESULTS AND ANALYSIS.....	24
6.1 Results of Image Analysis.....	24
6.2 Crack Evolution and Stress-Strain Relation - An Example of Simulation.....	24
6.3 Simulated Stress-Strain Relations, Experimental Results, and Comparison of the Two.....	30
7. DISCUSSIONS.....	44
8. CONCLUSIONS.....	49
9. ACKNOWLEDGEMENT.....	50
10. REFERENCES.....	51

For	
I	<input checked="" type="checkbox"/>
1	<input type="checkbox"/>
on	<input type="checkbox"/>
By	
Distribution/	
Availability Codes	
Dist	Avail and/or
A	Special

# 1. INTRODUCTION AND SUMMARY

## 1.1 Introduction

Fiber-reinforced ceramic composites offer the advantages of advanced ceramics (high-temperature capability, low density, oxidation and corrosion resistance) coupled with a non-catastrophic failure behavior. Application of this new class of structural materials, however, requires a new design philosophy that is based on their damage tolerance. In this context, the damage tolerance may be defined as the ability of the component to sustain crack-like defects that originate in processing as well as those that are introduced in service. It is equally important to understand the progress of damage, i.e. increase in the number and size of the crack-like defects with increasing load or time, in order to be able to predict 'safe' loads for sustainable limiting damage. Ceramic-matrix composites can be vulnerable to embrittlement by environmental interaction if the total damage exceeds a critical level and continuous paths are opened to the fiber-matrix interfaces via the linking of the cracks[1].

The initial damage in ceramic-matrix composites often occurs in the matrix because the failure strain of the matrix is typically much smaller than the failure strain of the fibers. Accordingly, much of the attention in modeling damage resistance of ceramic-matrix composites has been focused on matrix cracking[2]. In particular, micromechanics and fracture mechanics theories have been developed to model the critical stress for extension of preexisting, fully-bridged matrix cracks. The classical theory of Aveston, Cooper and Kelly[3] and the theory of Budiansky et al.[4] used energy balance analyses of steady-state cracks to define lower-bound matrix-cracking stress. Although these theories were based on sound fundamental principles, the restriction of steady-state cracks, i.e. long fiber-bridged cracks with uniform crack opening, makes them less useful for treating realistic, small-size cracks. Subsequent attention in modeling, therefore, shifted to calculating the critical stress for extension of small (non-steady-state) fiber-bridged cracks using the stress-intensity approach of fracture-mechanics theory[5-8].

All of the above theoretical analyses model the critical stresses for the unstable extension of fully-bridged cracks. Careful experiments conducted by Kim and Pagano[9] have recently revealed, however, that ceramic-matrix composites develop damage in the form of microcracks at applied stresses well below the observed proportional limits on the stress-strain curves, i.e. within the initial elastic regime. Further, these microcracks increase in number and size with increasing load. In the context of this picture of the

damage accumulation process, the transition from elastic to inelastic regime on the stress-strain curve is a consequence of the overall decrease in the elastic modulus of the composite due to bulk damage accumulation rather than due to the extension of a single fully-bridged crack.

A comprehensive design methodology for fiber-reinforced ceramic matrix composites should be based on mechanistic theories of damage, such as those matrix cracking theories noted above, in a framework that accommodates the 'probabilistic' and 'accumulative' aspects of the damage process[10]. Also, a conservative design philosophy should emphasize the use of damage initiation stress rather than the ultimate failure stress as a critical design parameter. At the present time, there is no established analytical tool for modeling the progressive damage process in fiber-reinforced ceramic matrix composites. The present Phase I research was aimed at developing a computational method for simulating the progressive damage and failure of fiber-reinforced composites under monotonic uniaxial loading. The computational method combines the existing knowledge of the fracture mechanics treatment of the stable growth of partially-bridged penny-shaped cracks with a size distribution of the fiber-free zones characterized from the microstructure of the composite. The size distribution of fiber-free zones is used as an input for the initiation of small matrix cracks within the gage section in the early stage of loading. Comparison of the predicted stress-strain curves with experimental results on selected composites was an essential part of this research.

## 1.2 Summary

A computational model was developed to simulate the progressive damage and failure of fiber-reinforced brittle matrix composites under uniaxial tensile loading. In conjunction with the basic material properties, this model used a size-distribution of the 'fiber-free zones' as an input for the development of small penny-shaped cracks at the early stage of loading. Stable extension of such non-steady-state cracks and the transition from non-steady-state to steady-state (cross-sectional) cracks were modeled using a stress-intensity formulation for a partially-bridged crack. The stress-intensity formulation made use of a force-displacement relation for the crack-bridging fibers and iterative numerical calculations for self-consistency of the bridging tractions and the crack-opening displacements. Stress-strain relation was simulated by calculating the total engineering strain in the gage section as a function of the applied stress. The total strain was obtained by summing the strains contributed from the non-steady-state and the steady-state cracks separately. Strain energies of the non-steady-state cracks and displacements of the fibers in the sliding zones of the steady-state cracks were calculated to estimate the total strain. Two unidirectional fiber-reinforced composites were investigated to test the predictive capability of this model. The fiber volume fractions, mean fiber radii, and size-distributions of the 'fiber-free' zones were characterized using stereological analysis of the microstructures of the composites. Material properties such as interfacial sliding stresses and matrix residual stresses were taken from the literature. The stress-strain relation predicted by the model was in good agreement with that measured experimentally for a SiC-reinforced calcium aluminosilicate composite. A SiC-reinforced magnesium aluminosilicate composite showed less cumulative strain before fracture due to premature fiber failure.



## 2. TECHNICAL BACKGROUND

A brief review of the current micromechanics theories is given in the following paragraphs. This will provide the background for the formulation of the progressive damage model, the subject of this research.

### 2.1 Critical Stress for Extension of Steady-State Matrix Crack

Aveston, Cooper, and Kelly[3] and Budiansky et al.[4] analyzed the critical stress for the extension of a steady-state crack using energy-balance approach. As shown in Figure 1, a large crack experiences a crack opening,  $u$ , which asymptotically approaches the steady-state maximum separation,  $u_0$ , of a matrix crack over the entire cross section. In a region far away from the crack tip, the total force in the intact fibers that bridge the crack per unit area exactly balances the far-field applied stress. The stress intensity at the crack tip is independent of the length of this steady-state crack zone and the stress needed to extend the crack is insensitive to the total crack length. Crack growth under this condition is referred to as steady-state growth. For composites with unbonded and frictional interfaces the critical stress for extension of the steady-state crack was formulated by Budiansky et al. as[4]:

$$\sigma_c = \sigma_0 - \frac{E_c}{E_m} \sigma_m^I \quad (1)$$

where

$$\sigma_0 = \left[ \frac{6 \tau G_m V_f^2 E_f E_c^2}{(1-V_f) E_m^2 R} \right]^{1/3} \quad (2)$$

where  $E_c$  is the Young's modulus of the composite determined by the rule of mixture (i.e.,  $E_c = E_f V_f + E_m V_m$ ),  $E_m$  and  $E_f$  are Young's moduli of the matrix and the fiber, respectively,  $\sigma_m^I$  is the axial residual stress in the matrix,  $G_m$  is the critical energy release rate for the matrix,  $V_f$  is the volume fraction of the fiber and  $R$  is the fiber radius.

Measurements performed on several glass- and glass-ceramic-matrix composites reinforced with SiC fibers showed that the matrix cracking stresses predicted by Eq. (1) were indeed close to the proportional limits measured on the stress-strain curves[11]. It is now known, however, that proportional limit on a stress-strain curve, i.e., the stress at the deviation from linear behavior, does not correspond to the extension of a single preexisting crack. It represents the cumulative effect of the stable growth of a large number of cracks on the compliance of the specimen. The critical crack extension stress predicted by Eq. (1)

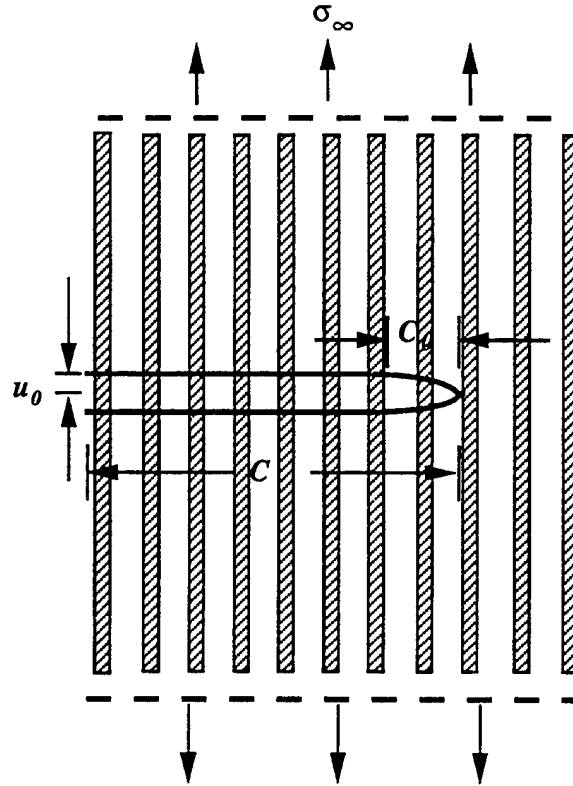


Figure 1. Schematic Representation of a Steady-State Matrix Crack in a Unidirectional Fiber-Reinforced Composite.

is generally considered as the lower bound of the matrix cracking stress of the pertinent composite.

## 2.2 Critical Stress for Extension of Short Cracks

For short cracks (as shown in Figure 2), the entire crack contributes to the stress intensity, and the stress required to propagate a crack is sensitive to the crack length. The critical stress for extension of a short (non-steady-state) crack in CMCs has been analyzed using the stress intensity approach by Marshall et al.[5], McCartney[6], Majumdar et al.[7], and recently Danchaivijit and Shetty[8,12]. The critical stress is calculated by equating the effective stress intensity for the matrix crack, i.e., the stress intensity obtained by superposing the contributions of the far-field stress and of the crack-bridging traction, with an effective fracture toughness ( $K_{IC}$ ) of the composite. The calculation requires an explicit relation between the crack-closure traction applied by the bridging fibers,  $p$ , and the crack-opening displacement,  $u$ .

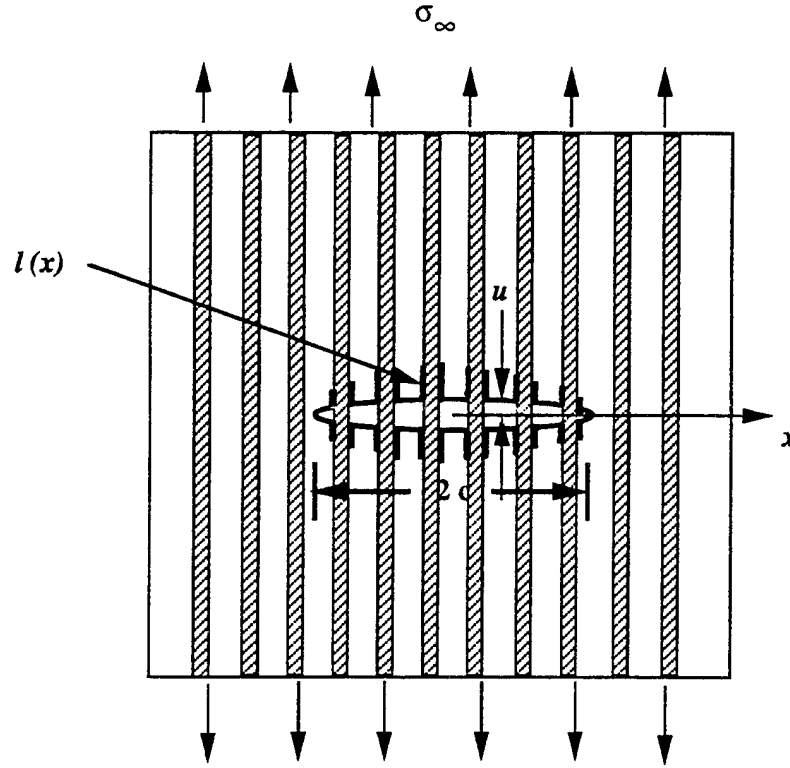


Figure 2. Schematic of a Short (Non-Steady-State) Crack Fully Bridged by Fibers.

We consider a small penny-shaped crack in an unbonded composite in which the sliding of matrix over the fibers is resisted only by frictional forces. By superposing the stress intensities caused by the far-field applied stress ( $\sigma_\infty$ ) on an unbridged crack and the crack closure distribution traction ( $p$ ) provided by the bridging fibers, the effective stress intensity of the crack,  $K$ , is obtained as [6,7]

$$K = 2 \left( \frac{c}{\pi} \right)^{1/2} \int_0^1 \frac{[\sigma_\infty - p(X)] X}{\sqrt{(1-X^2)}} dX \quad (3)$$

where  $X$  is the normalized position coordinate,  $x/c$  (see Figure 2).

For composites with unbonded, frictional interface, Danchaivijit et al. [8,12] have developed the following force-displacement relation for crack-bridging fibers:

$$p(X) = \frac{\eta \sigma'}{2(1+\eta)} \left\{ \sqrt{1 + \frac{4(1+\eta)u(X)}{\eta^2 u_0}} + 1 \right\} - \sigma_m^I V_m (1+\eta) \quad (4)$$

where  $\eta$  is equal to  $E_f V_f / E_m V_m$ ,  $V_m$  is the volume fraction of the matrix,  $\sigma' = \sigma_\infty + \sigma_m^I V_m (1 + \eta)$ . It has been shown in Ref. [8] that equivalence of the energy-release rates for steady-state cracks in the stress-intensity approach and the energy-balance theory of Budiansky et al.[4] suggests that  $u_0$  must be defined by the following equation:

$$u_0 = \frac{\sigma'^2 R}{2(3\eta + 2) E_f V_f^2 \tau} \quad (5)$$

In Eq. (4), when the crack-closure distribution traction,  $p$ , approaches the far-field applied stress,  $\sigma_\infty$ , the crack opening ( $u$ ) approaches  $u_0$ . When the crack-opening ( $u$ ) approaches zero, Eq. (4) predicts a lower limit of  $p$  equal to the far-field fiber stress.

In the  $p - u$  relation given above, the crack opening ( $u$ ) at a given position, however, is dependent on the entire distribution of the surface traction[13], for example,

$$u(X) = \frac{4(1-\nu^2)c}{\pi E_c} \int_X^1 \frac{1}{\sqrt{s^2 - X^2}} \int_0^s \frac{[\sigma_\infty - p(t)]t}{\sqrt{s^2 - t^2}} dt ds \quad (6)$$

for a penny-shaped matrix crack. Thus, it is essential to ensure that the crack-opening displacement,  $u(X)$ , and the crack-bridging traction,  $p(X)$ , are self-consistent before the stress intensity for the fiber-bridged crack is evaluated from Eq. (3). The numerical method suggested by Marshall et al.[5] to calculate the self-consistent crack-opening displacement function,  $u(X)$ , and the crack-bridging traction distribution,  $p(X)$  was used in the present model.

### 2.3 Fracture Criterion

The critical stress for extension of a fiber-bridged crack is obtained by combining Eq. (4) (with the self-consistent  $p(X)$ ) and an appropriate fracture criterion. Several different fracture criteria have been used in the literature to define the critical condition for extension of a fiber-bridged crack[5-7]. A critical energy release rate criterion was used in this study.

The fracture criterion was developed by equating the critical value of the energy release rate,  $G_c$ , expressed in terms of the critical composite stress intensity ( $K_c$ ) to the effective surface energy dissipated[6]:

$$G_c = \frac{K_c^2 (1-\nu^2)}{E'} = 2 V_m \gamma_m \quad (7)$$

where  $\nu$  is the Poisson's ratio of the composite and  $\gamma_m$  is the specific surface energy of the matrix.  $E'$  is a pertinent effective elastic modulus that depends upon the elastic anisotropy of the composite. Explicit expression for  $E'$  is given in Ref. [8]. Equation (7) can be rewritten in terms of the fracture toughness of the matrix,  $K_{cm}$  :

$$K_c = K_{cm} \left[ \frac{E' V_m}{E_m} \right]^{1/2} \quad (8)$$

The  $p - u$  relation described in Eqs. (4) and (6) in conjunction with the stress intensity calculation (Eq. (3)) and the fracture criterion (Eq. (8)) provided the basis for formulating the stable crack growth of partially-bridged penny-shaped cracks in the present study.

### 3. RESEARCH OBJECTIVES

The present Phase I research had the following objectives:

- (i) Develop a computational method for modeling the progressive damage and failure of fiber-reinforced ceramic matrix composites. Use this method to simulate the damage accumulation process and predict the stress-strain relations of unidirectional composites under monotonically increasing load.
- (ii) Compare the theoretical predictions with the experimental results from uniaxial tensile tests on two ceramic-matrix composites.

## 4. TECHNICAL APPROACH OF THE MODEL

### 4.1 Model of Crack Evolution

The present model assumed that small matrix cracks were initiated within the fiber-free zones (FFZs) and were arrested by the surrounding fibers in the early stage of loading. Figure 3A schematically illustrates how an internal penny-shaped crack, with radius  $a$ , is developed within a FFZ. The FFZs are caused by the non-uniform distribution of the fibers in the composite. Figure 3B shows the subsequent evolution of such matrix cracks. The initiated matrix crack can grow stably with increasing applied stress because of the increasing closure traction applied by the bridging fibers. Such cracks are referred to as partially-bridged matrix cracks or non-steady-state cracks. A partially-bridged matrix crack can extend stably until a critical applied stress is reached. At that stress level, the crack becomes unstable and extends throughout the entire cross-section of the composite specimen. Such cracks are referred to as steady-state cracks or cross-sectional cracks. Stable extension of the non-steady-state cracks and the transition from the non-steady-state to the steady-state cracks were modeled using a stress-intensity formulation for a partially-bridged crack. The stress-intensity formulation made use of the force-displacement relation described in Eqs. (4) and (6) and iterative numerical calculations for self-consistency of the bridging traction and the crack opening displacement. The fracture criterion described in Eq. (8) was used to calculate the crack extension stress.

### 4.2 Materials Properties

Two unidirectional fiber-reinforced glass-ceramic composites, SiC(Nicalon)-CAS (calcium aluminosilicate) and SiC(Nicalon)-MAS.5 (5% BSG-doped magnesium aluminosilicate), were selected for investigation in this research. Table 1 lists the material properties that were used in the theoretical calculations and their sources. For the SiC-CAS material, the coefficient of thermal expansion (CTE) of the matrix is higher than that of the fiber; thus the matrix is subject to tensile residual stress in the axial direction. On the other hand, in the SiC-MAS composite, the CTE of the matrix is lower than that of the fiber and, therefore, the matrix is subject to compressive residual stress. Other properties such as fiber radius ( $R$ ), fiber volume fraction ( $V_f$ ), and the size distribution of the FFZs were characterized using image analysis and are discussed in the next section.

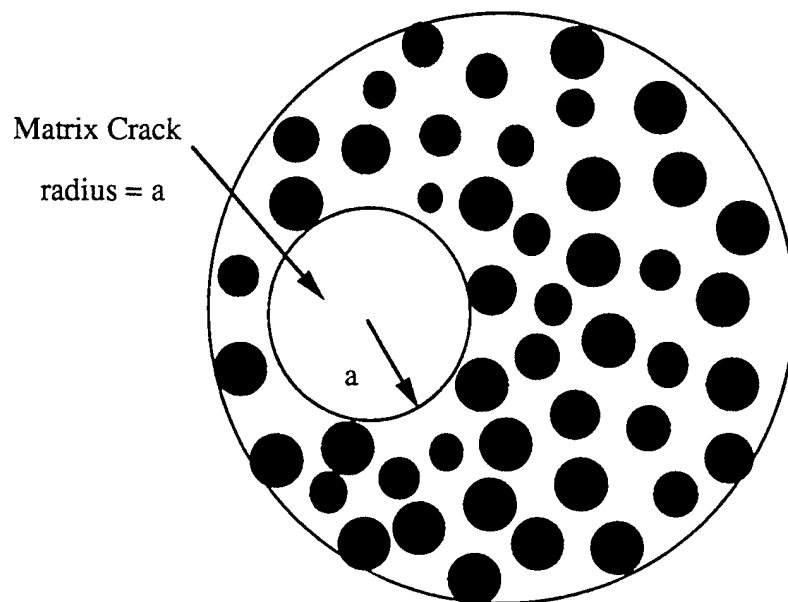
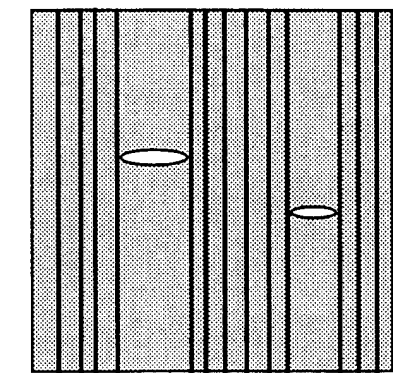
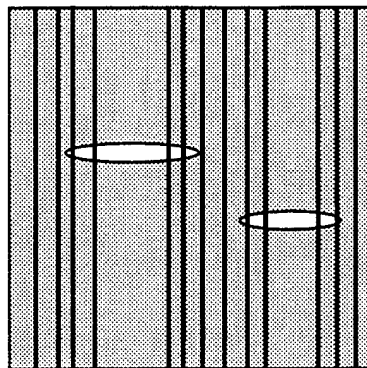


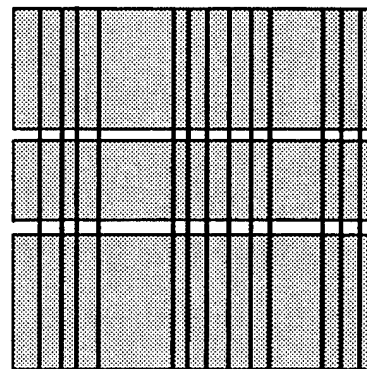
Figure 3A. Penny-Shaped Crack Initiated within a Fiber-Free Zone.



(1). Penny-Shaped Cracks Initiated in the Fiber-Free Zones



(2). Stable Extension of Partially-Bridged Penny-Shaped Cracks



(3). Cross Sectional Cracks after Unstable Extension

Figure 3B. Schematic Illustration of the Crack Evolution Model.



Table 1. Materials Properties Used in the Theoretical Calculation

Properties	SiC/CAS	SiC/MAS.5
<u>Coef. of Thermal Expansion</u> ( $\times 10^{-6}/^{\circ}\text{C}$ ) <sup>¶</sup>		
Fiber ( $\alpha_f$ )	4.0	4.0
Matrix ( $\alpha_m$ )	5.3	2.5
$\Delta T$ ( $^{\circ}\text{C}$ )	1100	1000
<u>Elastic Modulus</u> (GPa) <sup>¶</sup>		
Fiber ( $E_f$ )	200	200
Matrix ( $E_m$ )	97	124
<u>Poisson's Ratio</u>		
Fiber ( $\nu_f$ )	0.2	0.2
Matrix ( $\nu_m$ )	0.2	0.2
Matrix Fracture Toughness, $K_{\text{cm}}$ , ( $\text{MPa}\sqrt{\text{m}}$ )	1.63 <sup>§</sup>	2.38 <sup>§§</sup>
Matrix Residual Stress, $\sigma_m^I$ (MPa)	$89 \pm 13$ <sup>§</sup>	-102 <sup>*</sup>
Interfacial Sliding Stress, $\tau$ (MPa)	19 <sup>§</sup>	40 <sup>#</sup>

¶ Corning Inc. (Dr. K. Chyung).

§ D.S. Beyerle, S. M. Spearing, F. W. Zok, and A. G. Evans, *J. Am. Ceram. Soc.*, **75** [10] 2719-25 (1992).

§§ Measured in the present study using chevron-notched short-bar specimens.

# Private communication with Dr. F. Heredia and Mr. J. McNulty of University of California, Santa Barbara (unpublished work).

\* Theoretical estimation (using the equations proposed by B. Budiansky, J. W. Hutchinson, and A. G. Evans, *J. Mech. Phys. Solids*, Vol. **34** [2], 167-189, 1986).

#### 4.3 Characterization of the Microstructure and the Fiber-Free Zones

Five rectangular specimens of each composite, each measuring 5 x 4 x 3 mm, were cut from the same panel from which the tensile specimens were machined. The planes perpendicular to the unidirectional fibers were ground and polished. Figures 4A and 4B show the microstructures of the SiC-CAS and SiC-MAS composites, respectively. Quantitative evaluation of such microstructural parameters as mean fiber radius, fiber volume fraction, average fiber spacing, and size distribution of the FFZs were conducted using an image analyzing system<sup>1</sup> connected to an optical microscope.

<sup>1</sup> The software of this system was Vidas (version 2.1), Kontron System, Germany. The analysis was performed on a PC.

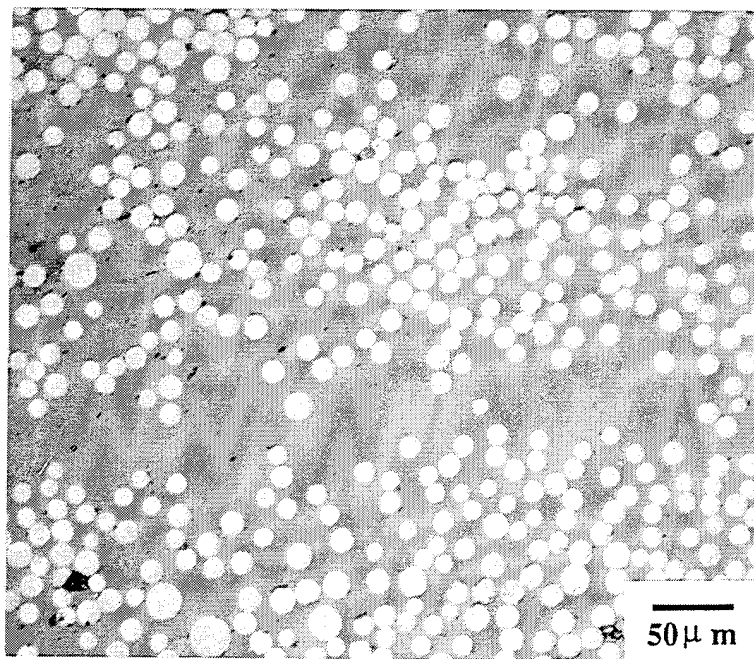


Figure 4A. Microstructure of the Nicalon-CAS Material.

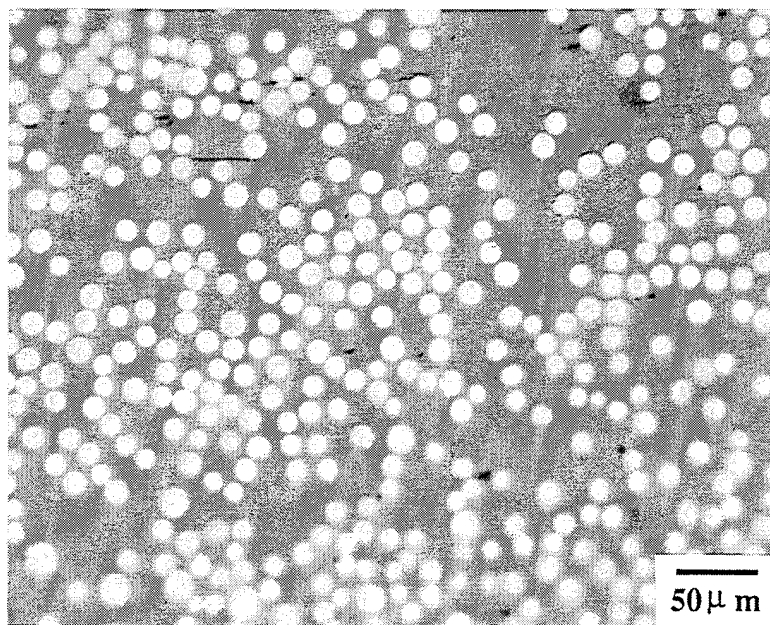


Figure 4B. Microstructure of the Nicalon-MAS Material.

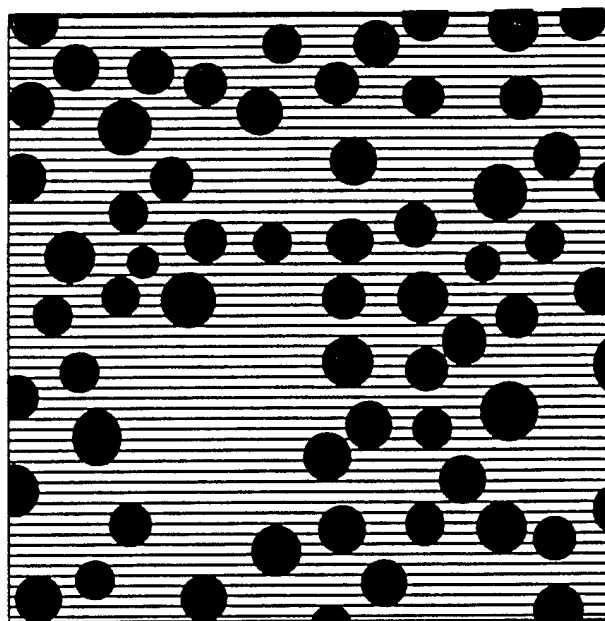


Figure 5. Schematic Illustration of the Quantitative Image Analysis.

The algorithms and the procedures of the image analysis used in the present study were developed by King and Schneider[14]. Figure 5 schematically illustrates how the microstructural parameters were evaluated. The area of each individual fiber and the average area fraction of the fibers was measured by producing sufficient contrast between the fiber and the matrix phases. The area of the fiber was converted to radius by considering a circle with equivalent area. The fiber volume fraction was considered to be equal to the area fraction characterized from these sectional planes. Twenty images (each image has the dimensions of  $244.7 \times 229.4 \mu\text{m}$ ) were sampled for each material to determine the fiber radius distribution and the average fiber volume fraction. To determine the average fiber spacing, the image analyzing system produced many parallel lines on the image and the length of each intercept in the matrix phase was measured. Approximately 6500 intercepts were measured for each composite material. The calculations of the fiber volume fraction and the average fiber spacing included a transformation procedure to correct the frame effect (i.e. larger fibers and longer intercepts were more likely to be cut off by the frame of the image, therefore, being underestimated).

A fiber-free zone was defined as a fiber-depleted region with the diameter of the maximum circle which could fit into the region being greater than the average fiber spacing. The size of a fiber-free zone was defined by its radius indicated as 'a' (as shown in Fig. 3A). Due to the limited time and resources in the Phase I research, determination of the size distribution of the FFZs was carried out manually by circling out all the possible FFZs on the image printouts<sup>2</sup>. The probability density of the FFZ as a function of the size was plotted as a histogram with an interval of 2.5  $\mu\text{m}$ , and the sampling action was continued until the distribution of the FFZs did not change significantly with more data. A total of 300 FFZs (from 25 images) were measured to determine the size distribution for each composite. The density distribution was then transformed to the cumulative distribution. The following cumulative distribution function, modified from the two-parameter Weibull Distribution function, was used to fit the measured data:

$$F(a) = 1 - \exp \left[ - \exp \left( B_1 + B_2 \ln(a) + B_3 (\ln(a))^2 + B_4 (\ln(a))^3 \right) \right] \quad (9)$$

In Eq. (9), the parameters  $B_1$ ,  $B_2$ ,  $B_3$ , and  $B_4$  were determined by fitting a polynomial to the data plotted as  $\ln(a)$  vs.  $\ln \ln[1/(1-F)]$ . In addition to the size distribution, the total number of fiber-free zones per unit area (area density) was also determined.

#### 4.4 Distribution of Fiber-Free Zones in the Gage Section of the Composite

Progressive matrix cracking with increasing applied stress results in a periodic crack array in the gage section of the composite. The crack spacing reaches a saturation value,  $S$ , when the cracks interact with one another, reducing the driving force for propagation of additional cracks. The magnitude of the saturation crack spacing is a function of the interfacial sliding stress, properties of the fiber and of the matrix.

To simulate the eventual matrix blocks, the gage section of the composite specimen was first assigned a number of equally-spaced planes. The spacing between adjacent planes was set to be  $2l$  as suggested by Zok and Spearing[15] for non-interacting condition, where  $l$  is the sliding length associated with the steady-state cracks at an applied stress  $\sigma_\infty$ :

---

<sup>2</sup> With additional effort in computer programming, the probability of finding a fiber-free zone with radius  $a$  can be determined as a function of the radius using the digital image memory technique and a random coordinate selection process.

$$l = \frac{[\sigma_{\infty} + \sigma_m^I V_m(1+\eta)] R}{2(1+\eta) V_f \tau} \quad (10)$$

The total number of planes was determined by the gage length (GL) of the specimen which was covered by the extensometer and  $l$ :

$$N = \text{Nint} \left[ \frac{GL}{2l} \right] \quad (11)$$

where 'Nint' is an operator which selects the nearest integer of the real number being considered. The total number of the FFZs that was assigned to each plane was obtained by multiplying the cross sectional area of the gage section and the area density of the fiber-free zones. The size of each assigned fiber-free zone was randomly selected from the size distribution function using a random number generator. Specifically, the 'linear congruential method'[16] was used to generate pseudo-random numbers on a computer. Integer numbers were generated in the range of (0,121500); each number was normalized by 121500 to define a cumulative frequency. Since the smallest FFZs had their radius equal to half of the average fiber spacing (but not zero), there was a finite cumulative frequency defined by Eq. (9) below which no FFZ existed. Therefore, the initially selected frequency was proportionally redefined into the range where the FFZs existed using the following equation:

$$F = F_i (1 - F_0) + F_0 \quad (12)$$

where  $F$  and  $F_i$  were the redefined and the initially selected cumulative frequencies, respectively.  $F_0$  was the cumulative frequency below which no FFZ existed. According to Eq. (9), the size of the FFZ corresponding to ' $F$ ' was determined and assigned in the gage section. A random selection process was used to ensure that the size distribution of the assigned fiber-free zones was different from plane to plane, and thus simulated the non-uniform fiber alignment in these composites.

#### 4.5 Transformation of FFZs to Cracks and the Cracking Stress - Crack Size Relation

A model was needed to control the transformation of the fiber-free zones to cracks at various stress levels. An ideal methodology would incorporate the initial flaw-size distribution of the composite and then use a model to randomly combine the 'flaw-size' and the 'fiber-free zone size' distributions to predict the initiation of every penny-shaped crack. However, there is little information available on the initial flaw-size distribution in

fiber-reinforced brittle matrix composites. Recently, an attempt has been made to investigate the possible relation between the residual stress profile in the FFZ and the configuration of the surrounding fibers of unidirectional composites using finite element analysis[17]. Results have indicated, however, that there is no significant change of the stress profile due to different configuration of the surrounding fibers.

The following model was used in the present research to define the transformation of the FFZs to cracks. The model assumed that the size of a fiber-free zone had the major influence on the initiation process, i.e. larger fiber-free zones were weaker and they became cracks at lower stress levels. To clearly illustrate this model, consider the following equations:

$$K = 2 \left( \frac{c}{\pi} \right)^{1/2} \left\{ \int_0^1 \frac{\sigma_{\infty} X}{\sqrt{(1-X^2)}} - \int_q^1 \frac{p(X)X}{\sqrt{(1-X^2)}} \right\} dX \quad (13)$$

$$u(X) = \frac{4(1-\nu^2)c}{\pi E_c} \int_X^1 \frac{1}{\sqrt{s^2-X^2}} \left[ \int_0^s \frac{\sigma_{\infty} t}{\sqrt{s^2-t^2}} dt - \int_q^s \frac{p(t)t}{\sqrt{s^2-t^2}} dt \right] ds \quad (14)$$

Equations (13) and (14) are the expanded forms of Eqs. (3) and (6), respectively, where the contributions from the far-field stress ( $\sigma_{\infty}$ ) and the crack closure traction applied by the bridging fibers ( $p$ ) are now evaluated separately. When the initial crack is of the same size as the fiber-free zone as shown in the first step of Fig. 3B,  $q = 1$  in both equations (i.e. there is no contribution from  $p$ ); when the crack is partially-bridged as shown in the second step of Fig. 3B,  $q$  has a value in the range of (0,1) and this value represents the portion of the crack length which is not bridged. For fully bridged cracks (cross-sectional cracks),  $q = 0$  and Eqs. (13) and (14) reduce to their original forms.

Equations (13) and (14) in conjunction with the  $p$ - $u$  relation were used to calculate the cracking stress - crack size relation for a given initial crack size. Figure 6 shows the relations calculated for the SiC-CAS material. Material properties listed in Table 1 were used in the calculations. In curve I, for example, a crack of initial size,  $c = 40 \mu\text{m}$  and  $q = 1$ , can grow stably with increasing applied stress, due to the increasing resistance

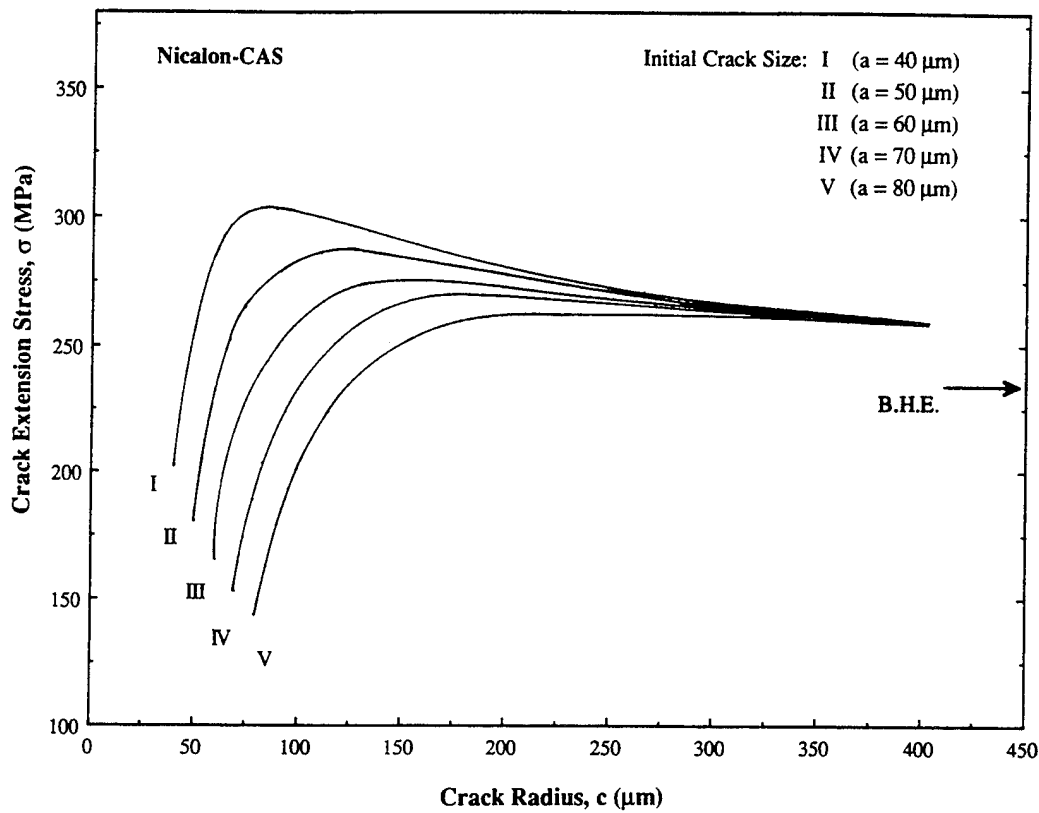


Figure 6. Cracking Stress - Crack Size Relation Calculated for the Nicalon-CAS Composite.

from the bridging fibers, up to 303.5 MPa. At this stress level, the crack becomes unstable since the cracking stress monotonically decreases with crack size and approaches the steady-state matrix cracking stress predicted by Budiansky et al.[4]. It is reasonable to assume that the crack extends through the entire cross section of the composite when the peak (unstable extension) stress is reached. It is also important to note that the peak stress decreases with increasing initial crack size, and the unstable extension occurs at a larger crack size if the initial crack size is larger.

In the transformation model used, a fiber-free zone with radius 'a' was assumed to transform to a crack of the same size when the applied stress reached the first matrix cracking stress, i.e. the first point of each curve in Fig. 6. In other words, this model assumed that small matrix cracks were initiated from nuclei within the fiber-free zones and then were arrested by the surrounding fibers during the early stage of loading. Following this model, larger fiber-free zones became cracks at lower stress levels, and the initial matrix cracking stress of a composite was strictly dependent on the size of the largest fiber-free zone which had been sampled and assigned to the gage section. This part will be addressed further in the results and analysis section.

#### 4.6 Simulation of the Stress-Strain Relation

The stress-strain relation was simulated by calculating the strain in the gage section as a function of the applied stress. The length of the gage section was equal to the gage length of the extensometer. The strains contributed from the non-steady-state and the steady-state cracks were considered separately. The total strain was equal to the sum of the two strains. For the non-steady-state cracks and the uncracked bulk subject to the far-field applied stress, a strain energy approach was used to first estimate the strain energy increase due to stable extension of the partially-bridged cracks, and the strain was calculated from the strain energy. For steady-state cracks, the fiber displacement within the sliding zones was calculated and normalized by the gage length to obtain the strain. Calculation steps are detailed in the following paragraphs.

*4.6.1 Strain of the Composite Subject to Far-Field Stress:* Assuming non-interacting cracks, the model considered the strain energy of a partially-bridged crack to be the strain energy of this crack when it was unbridged (i.e. all the fibers are broken) less the work done by the bridging fibers during partial crack closure:

$$W_c = \frac{8(1-\nu^2)\sigma_\infty^2 c^3}{3E'} - 2\pi c^2 \int_q^1 p(X) X [u_a(X) - u_b(X)] dX \quad (15)$$

In the above equation,  $\nu$  and  $E'$  are the Poisson's ratio and the effective elastic modulus of the composite, respectively;  $u_a(X)$  and  $u_b(X)$  are the crack opening displacements for the unbridged crack and the bridged crack, respectively. Since  $u_a(X)$  is greater than  $u_b(X)$ , the strain energy of a bridged crack is less than that of an unbridged crack. Figure 7 shows an example of the unbridged and the bridged profiles of a crack in a SiC-CAS composite that initiated at a FFZ 40  $\mu\text{m}$  in radius. The unbridged crack has a bigger crack opening than the partially-bridged crack. The crack closure traction distribution, at the applied stress of 276.7 MPa, is also shown in the figure.

The strain energy of a gage section containing many non-interacting and stably growing cracks was the total strain energy of all these cracks plus the strain energy of the uncracked body. The strain energy of cracks was the sum of the strain energies of each unbridged or partially-bridged crack:



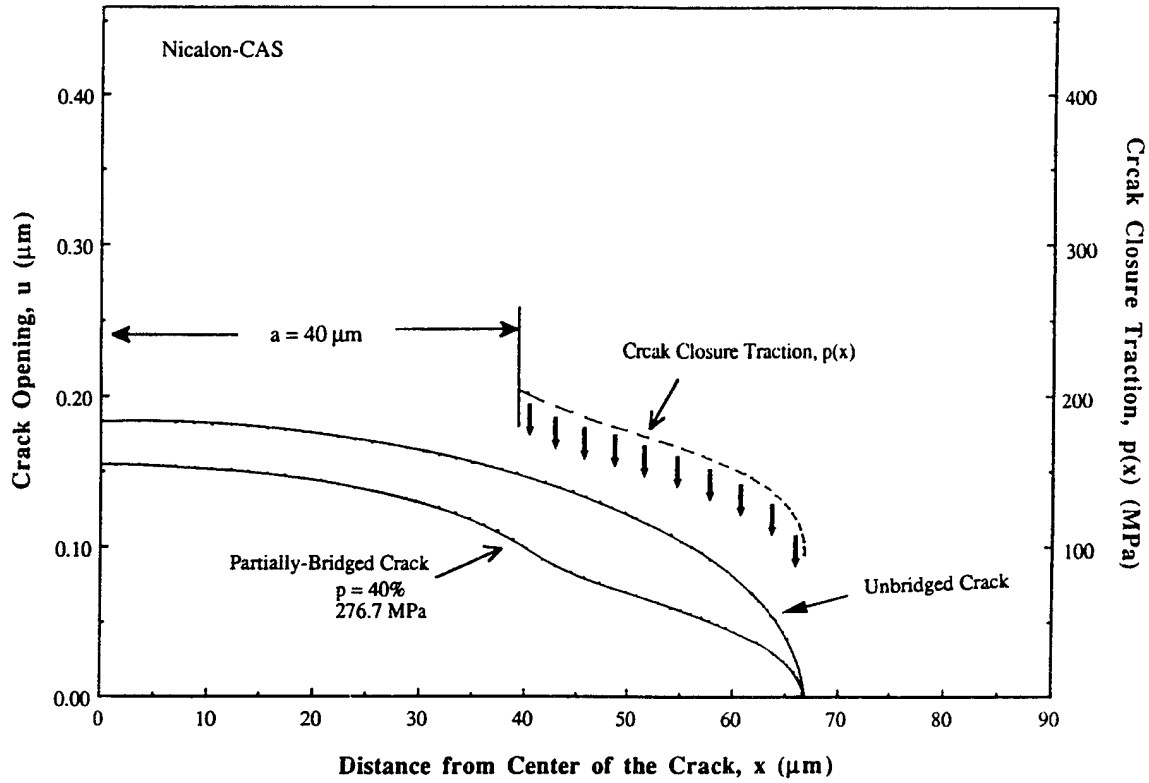


Figure 7. Comparison of the Crack Profiles of the Unbridged and the Bridged Cracks (calculated for the Nicalon-CAS material).

$$W_T = (N_1 W_{c1} + N_2 W_{c2} + \dots + N_i W_{ci}) + \left( \frac{\sigma_\infty^2}{2 E_c} \right) \quad (16)$$

where  $W_T$  is the total strain energy of a unit volume containing  $\sum N_i$  cracks at a stress level of  $\sigma_\infty$ ,  $W_{ci}$  is the strain energy of a bridged crack with crack length  $c = c_i$ ,  $N_i$  is the total number of cracks per unit volume with  $c = c_i$ .

When there were no steady-state cracks present in the gage section (this occurred when the specimen was in the early stage of loading), the stress-strain relation was simulated by first calculating the total strain energy increase ( $\Delta W_T$ ) in the gage section due to a small increment of the applied stress ( $\Delta \sigma_\infty$ ) and then convert the strain energy increase to strain increase ( $\Delta \epsilon$ ) using the following equations:

$$\Delta W_T = W_T(\sigma = \sigma_\infty + \Delta \sigma_\infty) - W_T(\sigma = \sigma_\infty) \quad (17)$$

$$\Delta \varepsilon = \frac{2 \Delta W_T}{\sigma_{\infty} + [\sigma_{\infty} + \Delta \sigma_{\infty}]} \quad (18)$$

At zero applied stress the gage section was considered to be uncracked. The gage section remained uncracked until the applied stress reached the first matrix cracking (the transformation) stress of the largest FFZ(s) present in the gage section. Before the largest FFZs transformed to cracks, the stress-strain relation was linear and the elastic modulus was equal to the composite modulus,  $E_c$ . When there were small cracks present in the gage section Eqs. (17) and (18) were repeatedly used to evaluate the stress-strain relation. The cumulative strain calculated in this step was denoted as  $\varepsilon_1$ .

*4.6.2 Strain Contributed from Steady-State Cracks:* When there were steady-state cracks present in the gage section the model shown in Figure 8 was considered. In this model, two sliding zones with equal sliding length,  $l$ , were present on either side of the crack. In addition to the strain contributed from the partially-bridged cracks and the uncracked body, strain was also contributed from the sliding zones of the steady-state cracks. Within the sliding zone, the displacement of the composite was equal to the displacement of the fibers.

$$\delta_c = \delta_f \text{ (over the sliding length)} \quad (19)$$

Thus, the strain of the composite in the sliding zone was readily assessed by calculating the displacement of the fibers. The total displacement of the fibers within the gage section was determined by the total number of sliding zones present in the gage section and the fiber displacement in each sliding zone:

$$\delta_{f,\text{total}} = 2 N_{ss} \delta_f \quad (20)$$

where  $N_{ss}$  is the total number of steady-state cracks within the gage length, and  $\delta_f$  is the displacement of the fibers within one sliding zone. The assumption of constant interfacial sliding stress results in the following expression for the fiber displacement in the sliding zone[8]:

$$\delta_f = \frac{\sigma_f}{E_f} l + \frac{\tau}{R E_f} l^2 \quad (21)$$

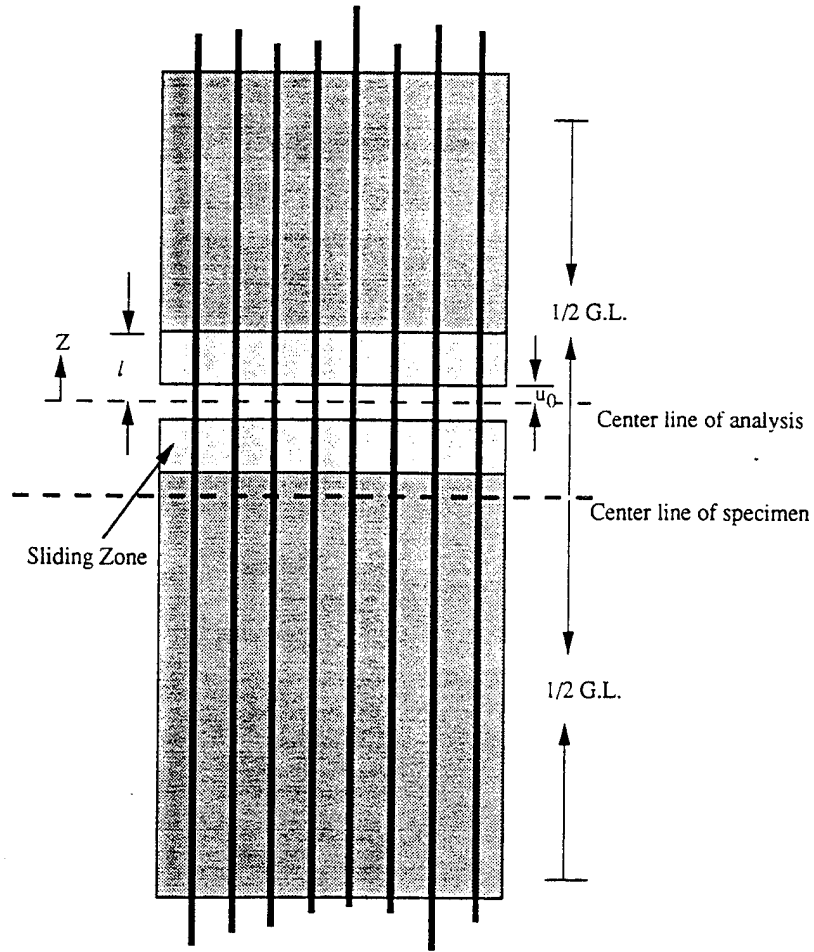


Figure 8. Model for Analyzing Steady-State Cracks.

where  $\sigma_f$  and  $l$  are defined in Eq. (5) and Eq. (10), respectively.

The strain in the sliding zones was calculated by normalizing the fiber displacement with the gage length and was denoted as  $\epsilon_2$ :

$$\epsilon_2 = \frac{\delta_c}{GL} = \frac{\delta_{f.total}}{GL} \quad (22)$$

The total strain, at a given applied stress, was obtained by summing the two contributions:

$$\epsilon = \epsilon_1 + \epsilon_2 \quad (23)$$

## 5. EXPERIMENTAL PROCEDURE

### 5.1 Specimen Preparation

The specimen configuration followed the specifications for edge-loading tensile tests developed by Holmes[18]. Figure 9 shows the specifications of the specimen. The thickness of the SiC-CAS specimens and the Nicalon-MAS specimens were 3.0 mm (16-ply panel) and 1.5 mm (8-ply panel), respectively. Specimens were polished using diamond compound paste before test.

### 5.2 Edge-Loading Tensile Test

The edge-loading test fixtures were mounted on a universal test machine<sup>3</sup>. Special care was taken to ensure proper alignment of the specimen with the load train[19]. Specimens were tested in air, room temperature and a crosshead speed of 0.2 mm/min. This crosshead speed translated to a stressing rate of 1.0 MPa/s for the SiC-CAS composite and 1.3 MPa/s for the SiC-MAS composite. The strain was measured with an extensometer using a gage length (GL) of 31.75 mm.

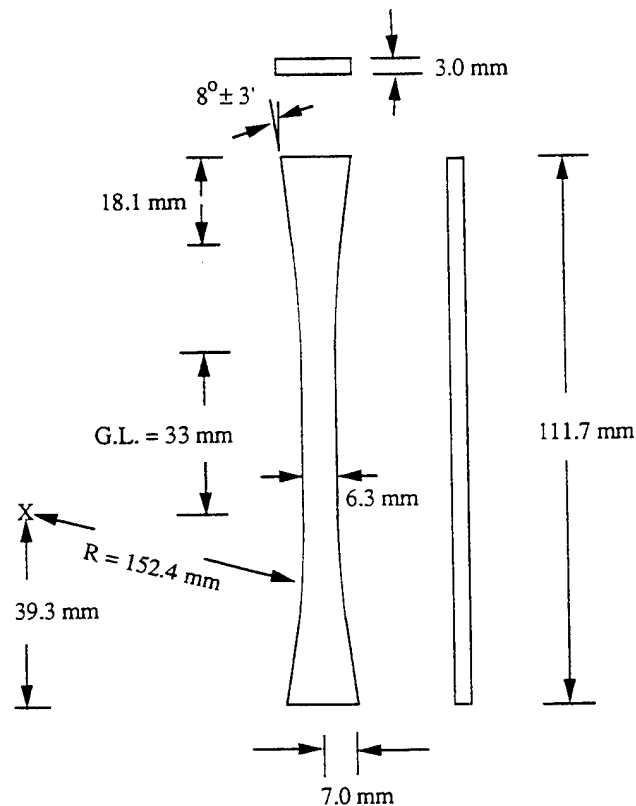


Figure 9. Specifications of the Edge-Loading Tensile Specimens.

<sup>3</sup> Model 4206, Instron Inc., Canton, MA.

## 6. RESULTS AND ANALYSIS

### 6.1 Results of the Image Analysis

Table 2 summarizes the microstructural parameters characterized using the image analysis of the two composites. The fiber volume fractions were determined to be  $V_f = 0.396$  and  $0.343$  for the SiC-CAS and the SiC-MAS composites, respectively. Figures 10 and 11 show the fiber radius distributions in the two composites. As can be seen, in both cases, the distributions could be well described by a normal distribution function; the calculated means and standard deviations are listed in Table 2. In addition, the average fiber spacings were measured to be  $19.1 \mu\text{m}$  and  $23.9 \mu\text{m}$  for the SiC-CAS and the SiC-MAS materials, respectively. The larger average fiber spacing of the SiC-MAS composite was consistent with the measured fiber volume fractions of the two composites.

Figure 12(A) shows the size distribution of the FFZs characterized from the SiC-CAS composite. The density distribution is plotted as a histogram with an interval of  $2.5 \mu\text{m}$ . Those small fiber-depleted regions ( $a \leq 10 \mu\text{m}$ ) were not measured since they were not qualified as FFZs. Figure 12(B) shows the size distributions of the FFZs in a cumulative distribution plot. For conservative design, the density distribution data was transformed to the cumulative distribution data based on the largest radius of each interval in the histogram. Equation (9) was fitted to the measured data, and the best-fit parameters were determined to be:  $B_1 = -30.315$ ,  $B_2 = 23.292$ ,  $B_3 = -5.8099$ ,  $B_4 = 0.5012$ .

Similarly, Figures 13(A) and 13(B) show the size distribution of the FFZs characterized from the SiC-MAS composite. The best-fit parameters were determined to be  $B_1 = -62.608$ ,  $B_2 = 55.812$ ,  $B_3 = -16.726$ ,  $B_4 = 1.7146$ . The two cumulative distributions appeared to be similar except that some large FFZs, with  $a = 42.5 \mu\text{m}$ , were sampled from the SiC-CAS composite but not from the SiC-MAS material. This led to a slightly faster saturation of the distribution function toward unity in the latter material. The area density of the FFZs was determined by normalizing the total number of FFZs that were sampled with the total imaged area; these values are listed in Table 2.

### 6.2 Crack Evolution and Stress-Strain Relation - An Example of Simulation

First, consider the hypothetical case where the FFZs in the gage section are of a uniform size ( $a = 80 \mu\text{m}$ ). This example will illustrate how the crack evolution and the corresponding stress-strain relation are simulated in the present model. Material properties

Table 2. Microstructural Properties Obtained from Image Analysis

Property	Nicalon-CAS	Nicalon-MAS
Fiber Volume Fraction ( $V_f$ )	0.396	0.343
Fiber Radius, $R$ ( $\mu\text{m}$ )	Normal Distribution $6.90 \pm 1.14$	Normal Distribution $6.50 \pm 0.73$
Average Fiber Spacing, $D_f$ ( $\mu\text{m}$ )	19.1	23.9
Size Distribution of Fiber-Free Zone, $F(a)$	Exponential Type Function	Exponential Type Function
Area Density, $\#/\text{m}^2$	$2.025 \times 10^8 / \text{m}^2$	$2.261 \times 10^8 / \text{m}^2$

of the Nicalon-CAS composite were used in the calculation. Figures 14 and 15 show the three important stages of development of a single crack and the corresponding stress-strain relation, respectively. In the first stage, the gage section remained uncracked until the applied stress reached the transformation stress of the defined FFZ (i.e. the first matrix cracking stress, 142.8 MPa). At this point, the FFZ transformed to a crack of the same size. The corresponding stress-strain curve is the linear portion from zero stress to point 'a'. In the second stage, with increasing applied stress, the crack grow stably with increasing applied stress, up to the maximum cracking stress (262.3 MPa). The corresponding  $\sigma - \epsilon$  relation for this stage is from 'a' to 'b'. The relation is not exactly linear, however, it appears to be linear since the additional strain energy contributed from the crack is too small as compared to the strain energy of the uncracked bulk. In the third stage, the crack becomes a cross-sectional crack and the subsequent stress-strain behavior is calculated according to the model illustrated in Fig. 8. The corresponding  $\sigma - \epsilon$  relation for this stage is indicated as the sudden increment of strain from 'b' to 'c' and the subsequent linear relation from 'c' to 'f'. Also plotted in Fig. 15 are the stress-strain relations for the gage section containing multiple (10 and 20) but non-interacting cracks developed from FFZs of the same size. Note that the slope of e-h is smaller than the slope of d-g, and the slope of d-g is smaller than the slope of b-f.

The logic and procedure described above were employed to simulate the stress-strain relation of the gage section of the composite. When the entire gage section was

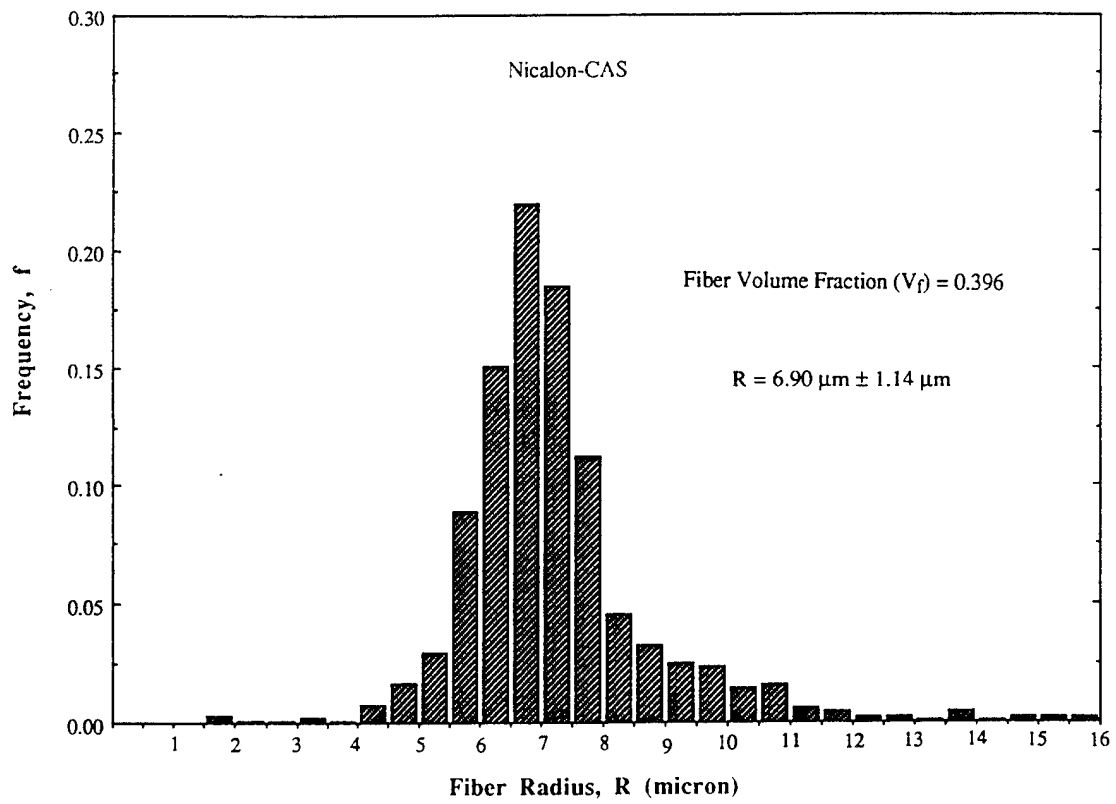


Figure 10. Fiber Radius Distribution of the Nicalon-CAS Composite.

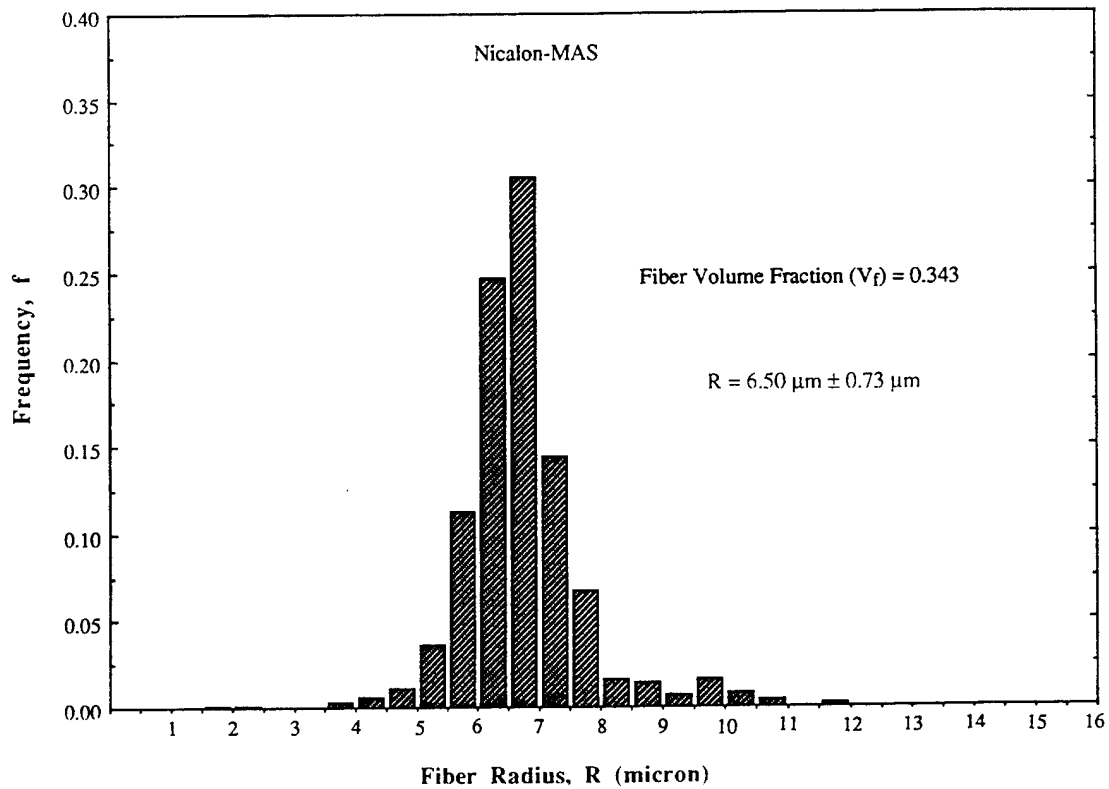


Figure 11. Fiber Radius Distribution of the Nicalon-MAS Composite.

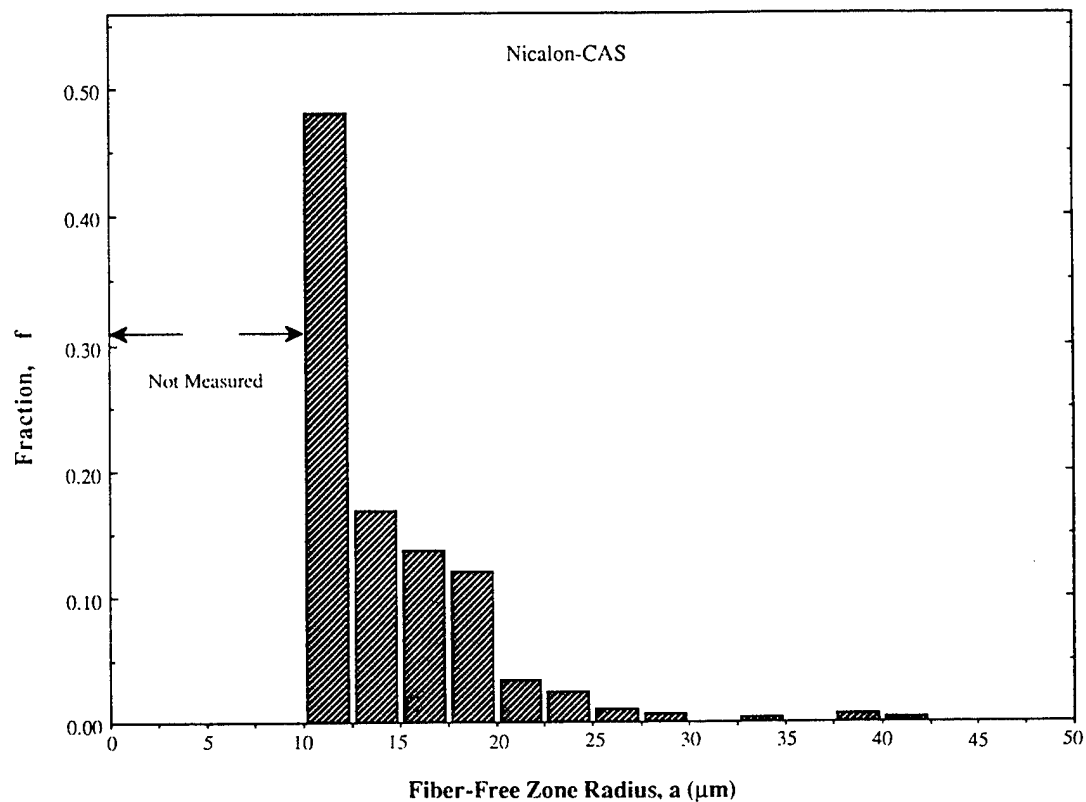


Figure 12(A). Density Distribution of the FFZ Radius (Nicalon-CAS).

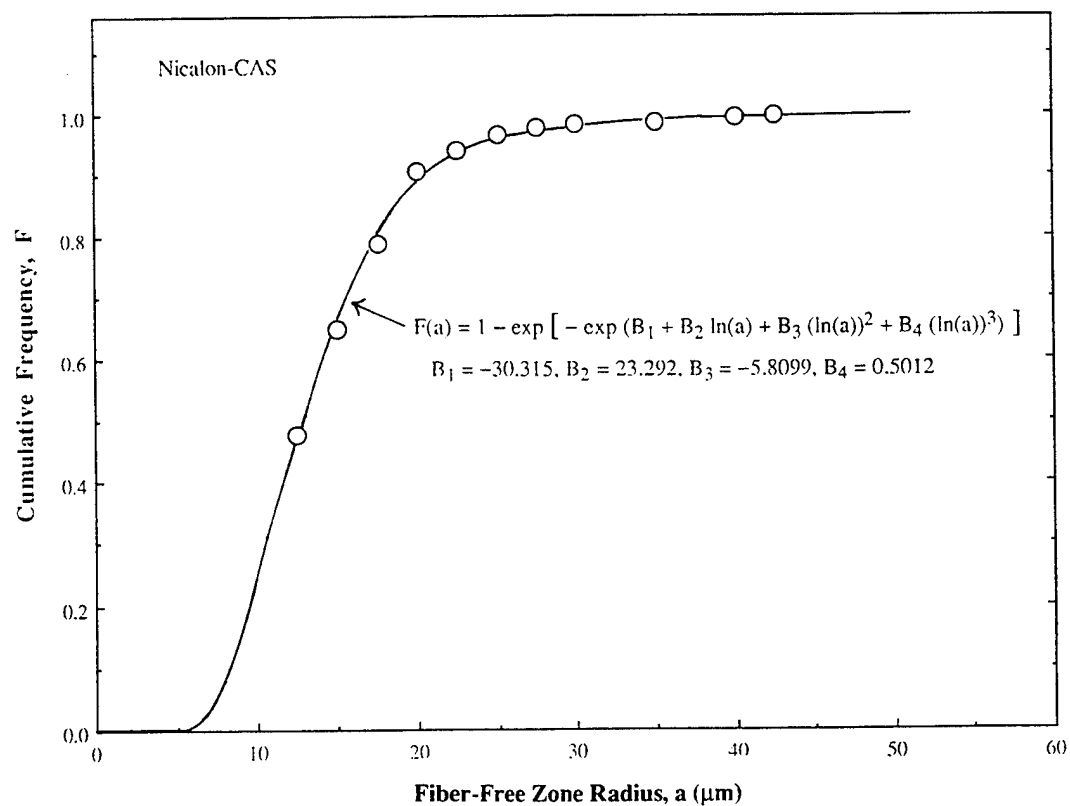


Figure 12(B). Cumulative Distribution of the FFZ Radius (Nicalon-CAS).



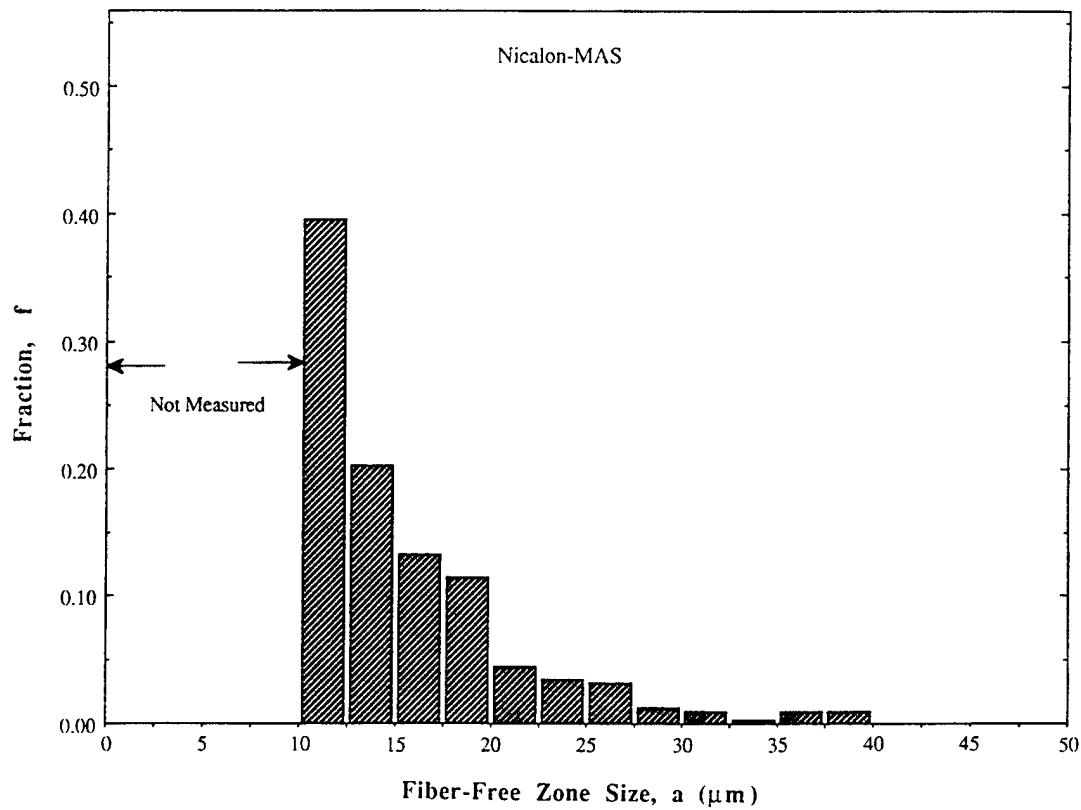


Figure 13(A). Density Distribution of the FFZ Radius (Nicalon-MAS).

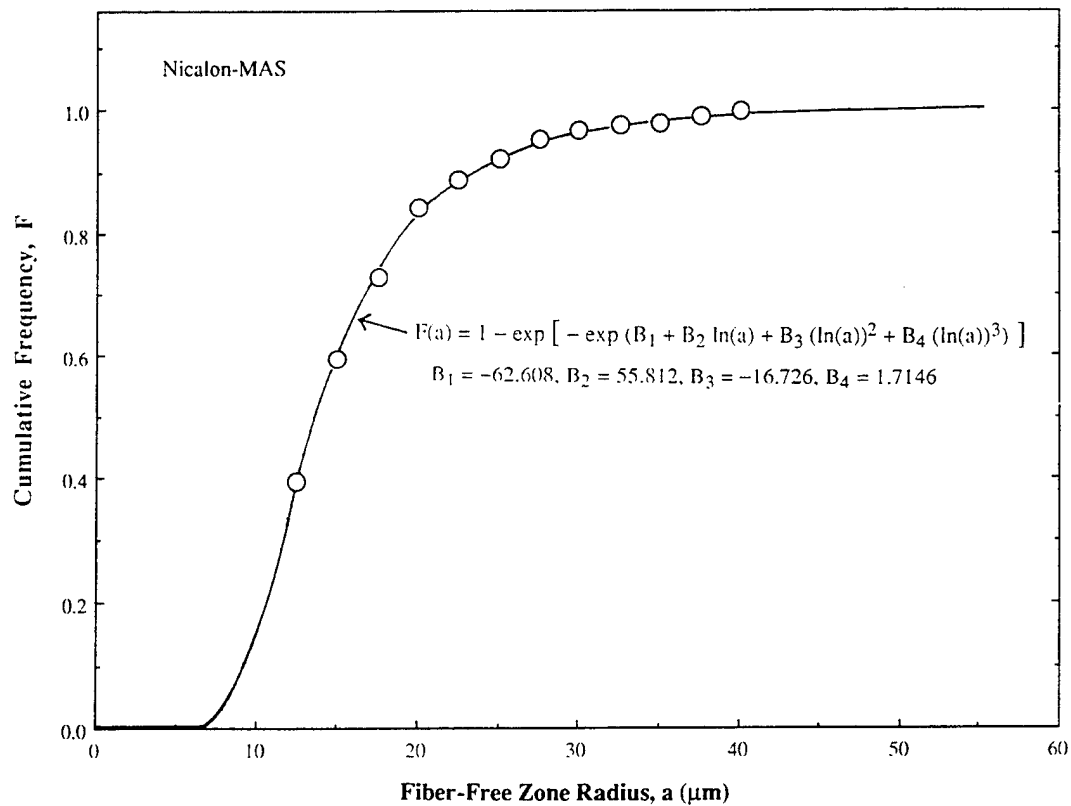


Figure 13(B). Cumulative Distribution of the FFZ Radius (Nicalon-MAS).

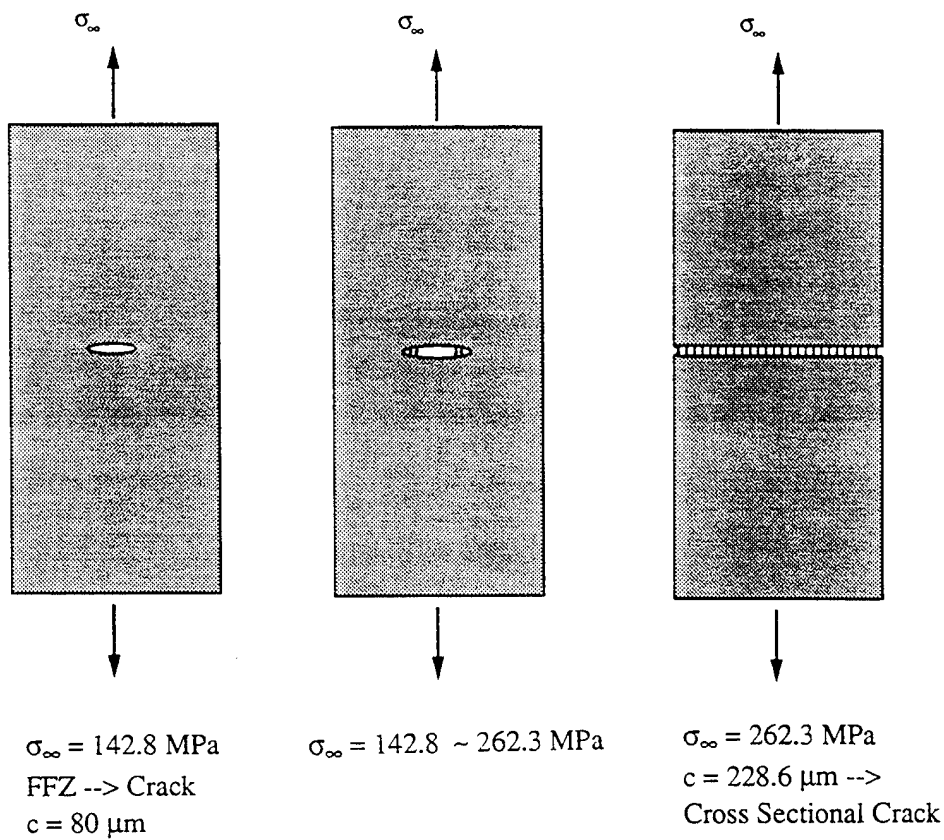


Figure 14. Crack Evolution of a Single Crack Developed from a 80  $\mu\text{m}$  Fiber-Free Zone.

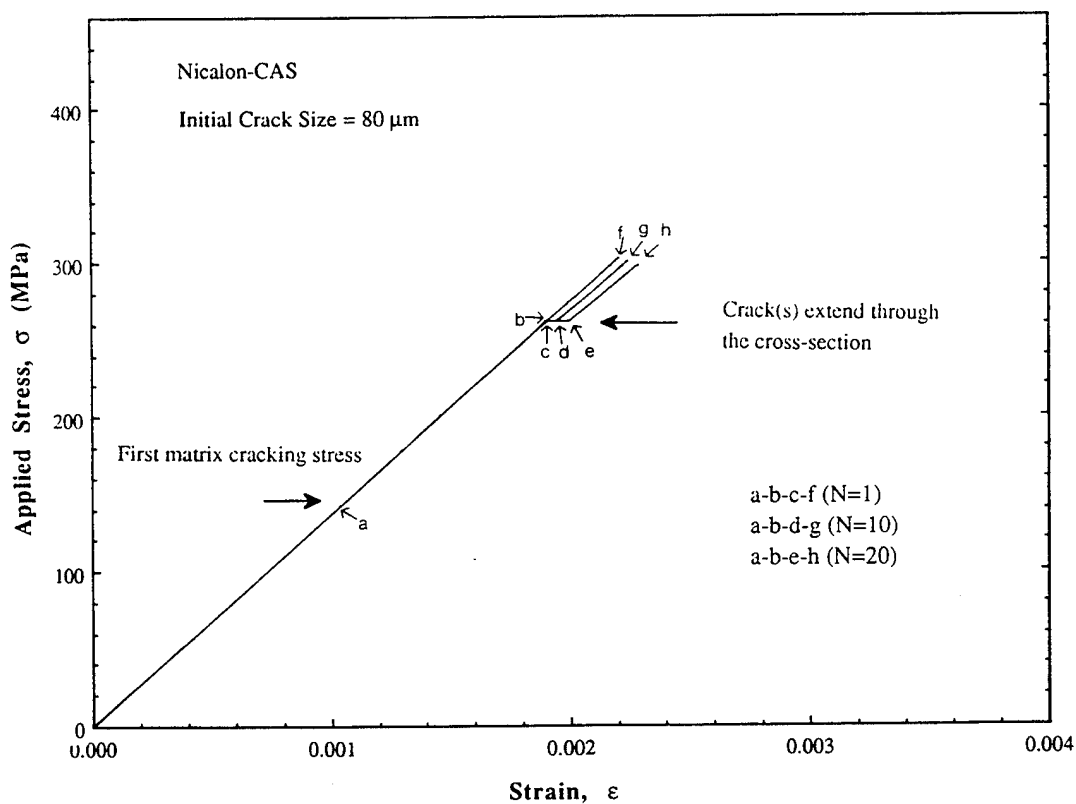


Figure 15. The Corresponding Stress-Strain Relation of Figure 14.

considered, there was a large number of FFZs with different sizes that transformed to cracks at various stress levels. The stress-strain behavior over the gage section due to this crack evolution process was computed based on two assumptions:

- (1). It was assumed that there was no interaction among the cracks developed on the same plane or on adjacent planes.
- (2). Within a plane, once the largest crack(s) became unstable, it extended through the entire cross section, and the other cracks on the same plane were deleted from the gage section.

### 6.3 Simulated Stress-Strain Relations, Experimental Results, and Comparison of the Two.

*6.3.1 SiC-CAS Composite:* Figures 16(a) through 16(f) schematically illustrate the crack evolution within the gage section of the SiC-CAS composite. These figures are explained as follows:

Fig. 16(a): Starting with an uncracked gage section, fiber-free zones of different sizes were distributed on equally spaced planes. Totally 228 planes were assigned to the gage section. Each plane contained 3827 FFZs. With increasing applied stress, the gage section remained uncracked until the applied stress reached the transforming stress of the largest FFZs present in the gage section. The largest FFZs which were sampled from the distribution function and assigned into the gage section were 87.5  $\mu\text{m}$  in radius, the transformation stress of such FFZs was 136.5 MPa.

Fig. 16(b): When the applied stress reached 136.5 MPa, the largest FFZs transformed to cracks of the same size. These cracks started stably extending into the surrounding fiber-reinforced regime.

Fig. 16(c): When the applied stress reached the transformation stress of the next largest FFZs present in the gage section (85.0  $\mu\text{m}$  in radius, 138.5 MPa), these FFZs became cracks. The gage section, at this time, contained both partially-bridged cracks and unbridged cracks. With increasing applied stress, the number of non-steady-state cracks kept increasing until the instability stress of the largest cracks was reached.

Fig. 16(d): At the stress level of 259.4 MPa, those cracks initiated from the 87.5  $\mu\text{m}$  FFZs were unstable and became steady-state cracks. At this point the gage section contained both steady-state and non-steady-state cracks.

Fig. 16(e): As the applied stress increased further, the number of steady-state cracks increased, and the number of non-steady-state cracks decreased.

Fig. 16(f): Eventually, the gage section was filled with equally spaced steady-state cracks. The number of steady-state crack was equal to the number of planes initially assigned into the gage length. No small cracks were present.

According to the crack evolution process described above, Figure 17 shows the average steady-state crack density as a function of the applied stress. The crack density was calculated by dividing the number of steady-state cracks in the gage section by the gage length at a specific stress level. The steady-state crack density gradually increased with applied stress and finally reached the defined saturation spacing.

Figure 18 shows the comparison of the predicted and the measured stress-strain relations of the SiC-CAS. The predicted relation is indicated by the dashed line. The predicted initial matrix cracking stress (136.5 MPa) was very close to the value (132 MPa) reported by Kim and Pagano[9] using acoustic emission. After the initial matrix cracking, the subsequent stress-strain relation appeared to be linear inspite of the hundreds of non-steady-state cracks that developed in the gage section. This was attributed to the small strain energy contributed by the cracks as compared to the strain energy of the uncracked bulk. The steady-state matrix cracking started at 259.4 MPa (by those cracks initiated from the 87.5  $\mu\text{m}$  FFZs), and completed at 285.8 MPa (by those cracks initiated from 50.0  $\mu\text{m}$  FFZs). After that, the stress-strain relation represented the tensile behavior of the gage section containing periodic matrix blocks. The measured stress-strain relation (indicated by the solid line), on the other hand, exhibited more gradual transition from the initial elastic regime to the inelastic regime due to matrix cracking. The initial elastic modulus was estimated to be 141.9 GPa, and based on that, the proportional limit was located at about 200 MPa. The lower bound steady-state matrix cracking stress (the BHE limit) was calculated to be 231 MPa, slightly higher than the proportional limit. The first steady-state matrix cracking stress predicted by the model was higher than the BHE model. In addition, the model gave reasonable prediction of the total inelastic strain due to matrix cracking. However, the predicted steady-state matrix cracking stresses were approximately 50 MPa lower than the experimental results. This discrepancy can be attributed to the uncertainty of the material properties such as matrix fracture toughness, residual stress, and the interfacial sliding stress. These aspects will be discussed later.

Nicalon-CAS  $\sigma_{\infty} = 0$  MPa

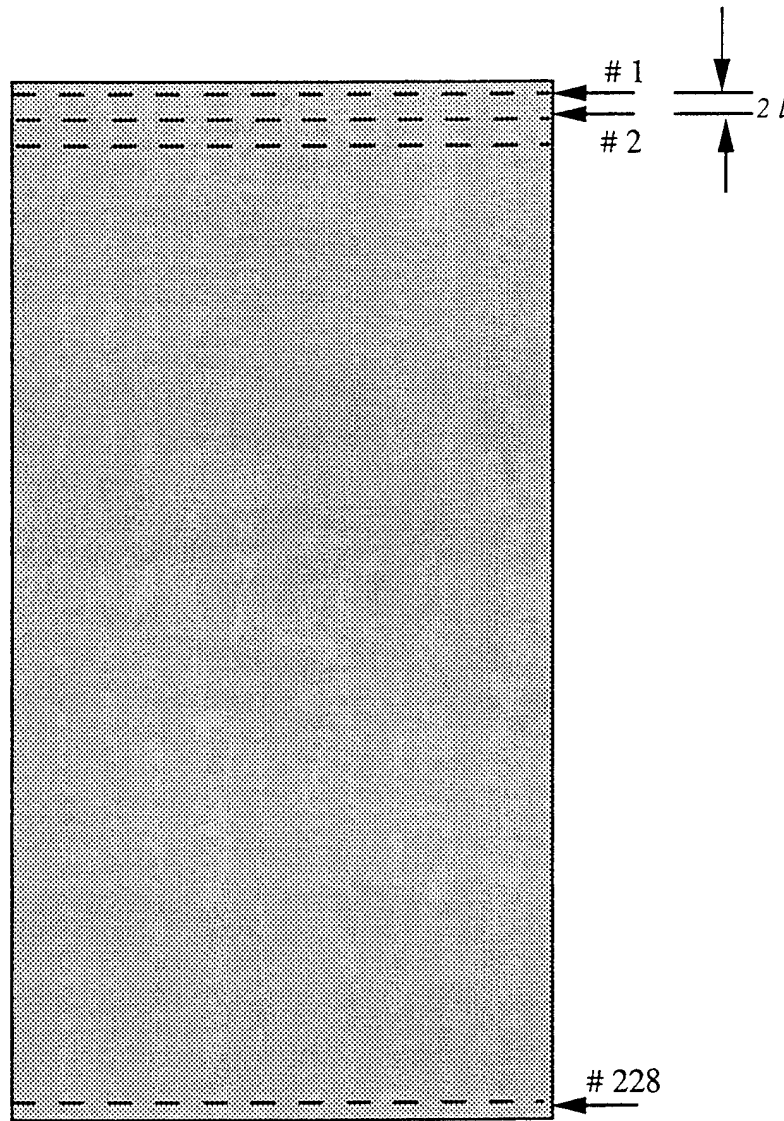


Figure 16 (a). Simulated Crack Evolution of Nicalon-CAS Composite.

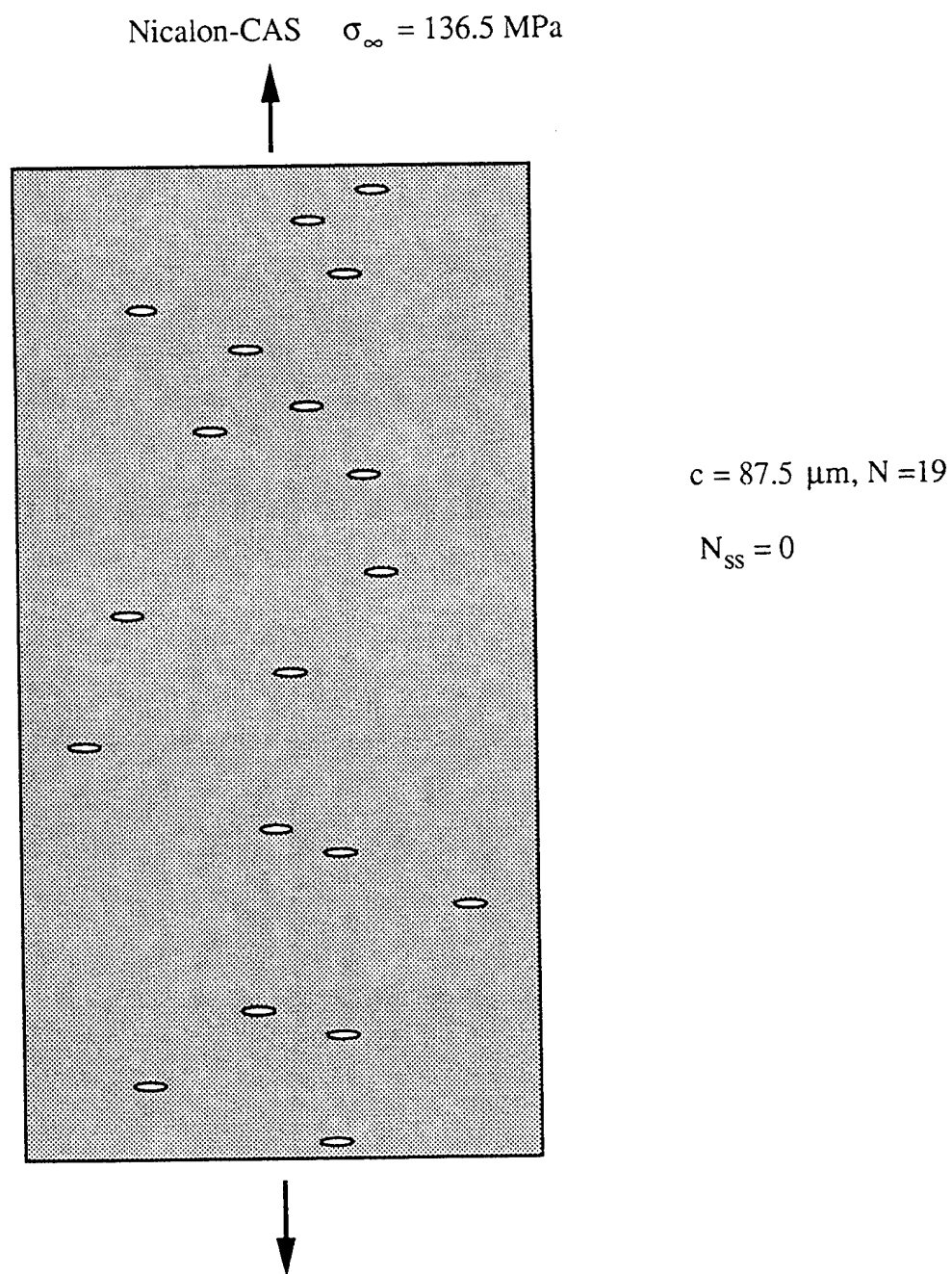


Figure 16 (b). Simulated Crack Evolution of Nicalon-CAS Composite - Continued.

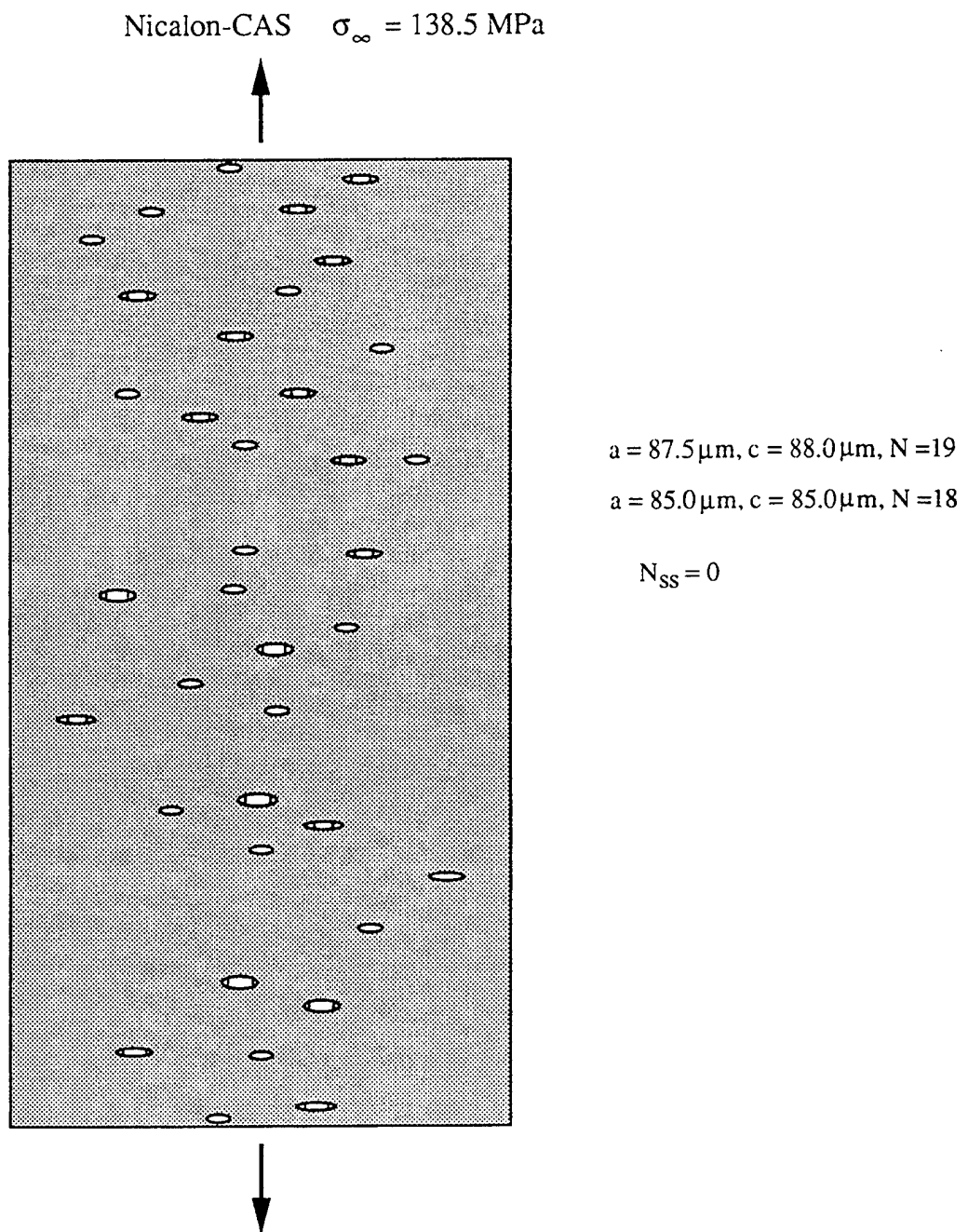


Figure 16 (c). Simulated Crack Evolution of Nicalon-CAS Composite - Continued.

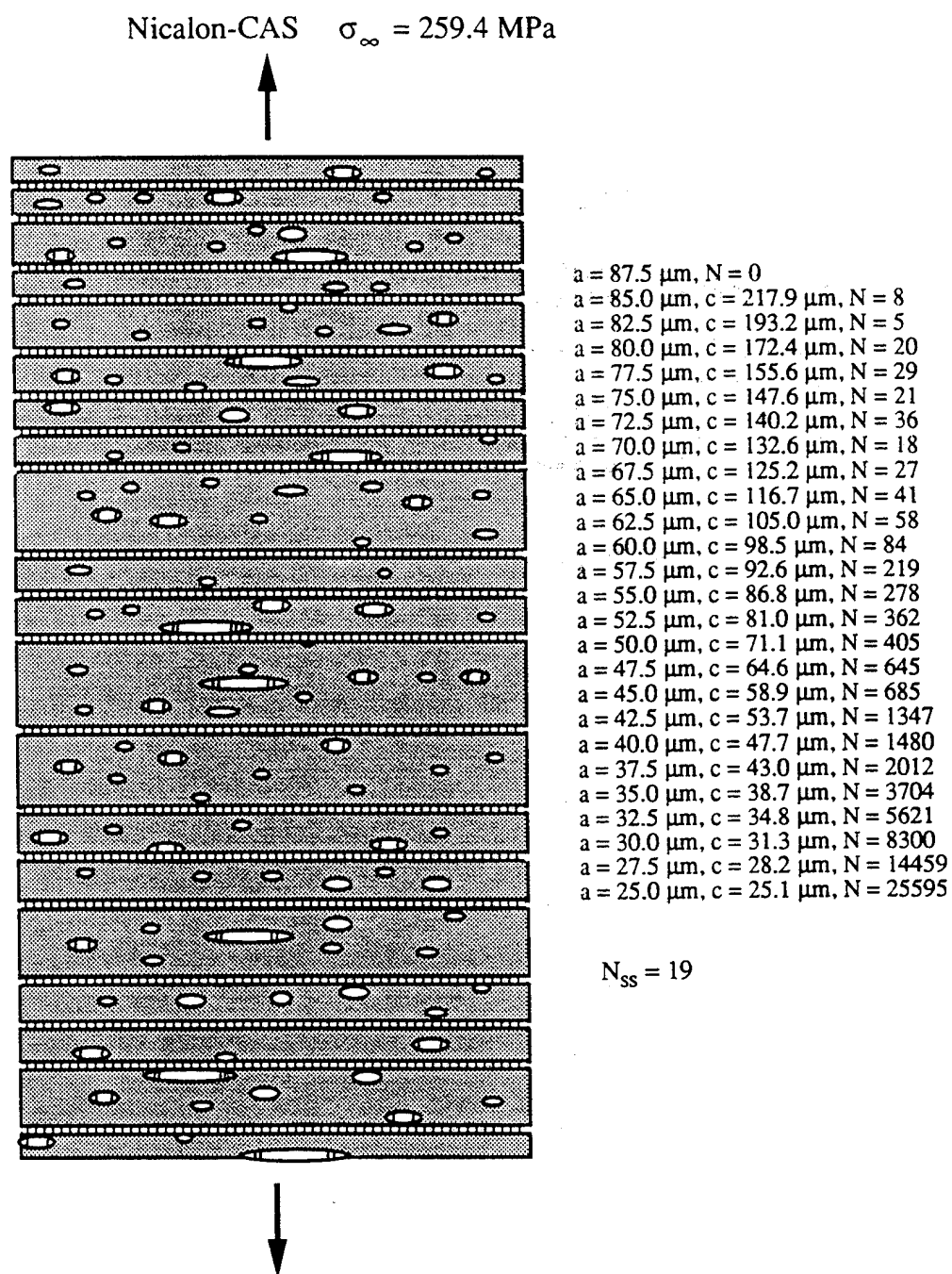


Figure 16 (d). Simulated Crack Evolution of Nicalon-CAS Composite - Continued.



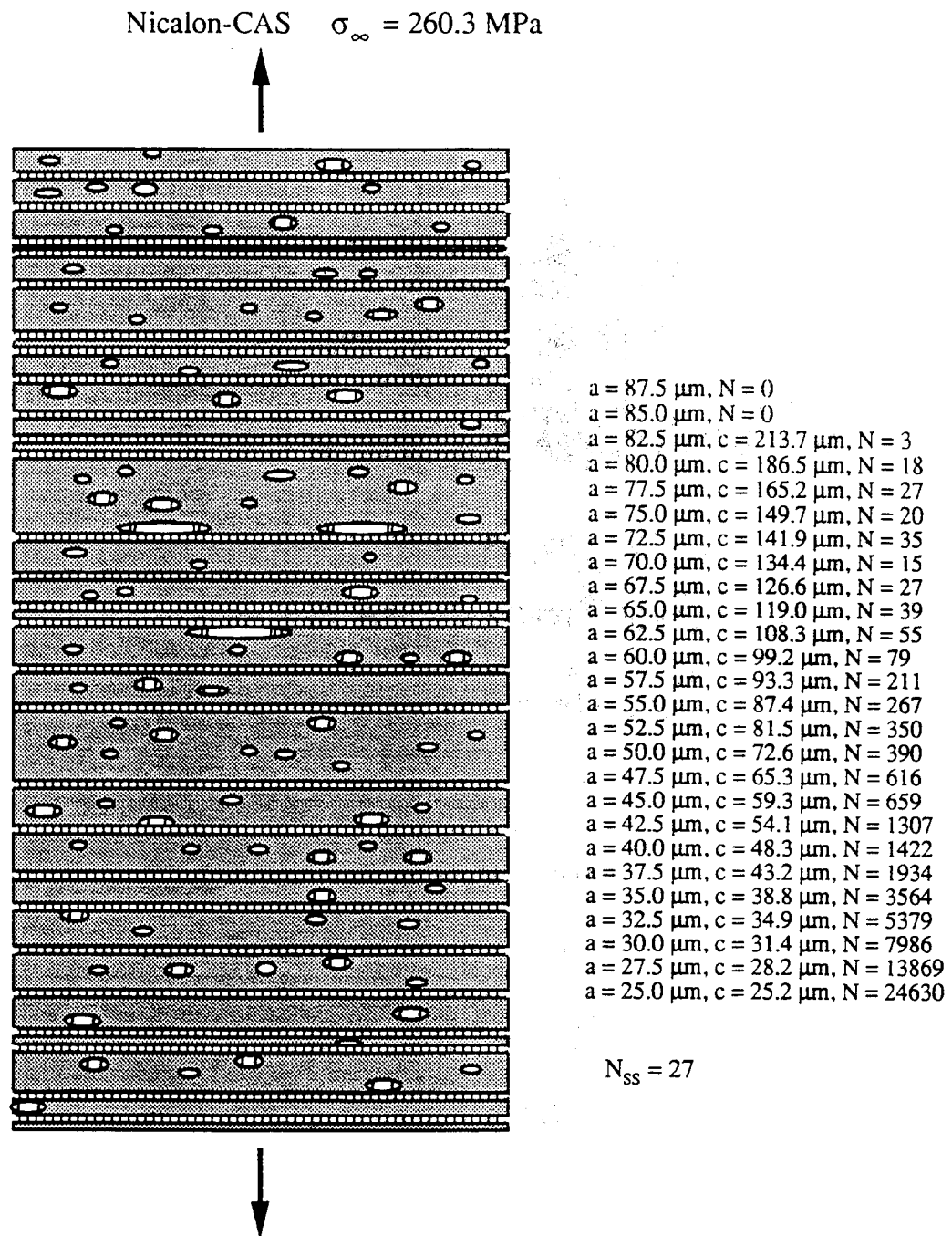


Figure 16 (e). Simulated Crack Evolution of Nicalon-CAS Composite - Continued.

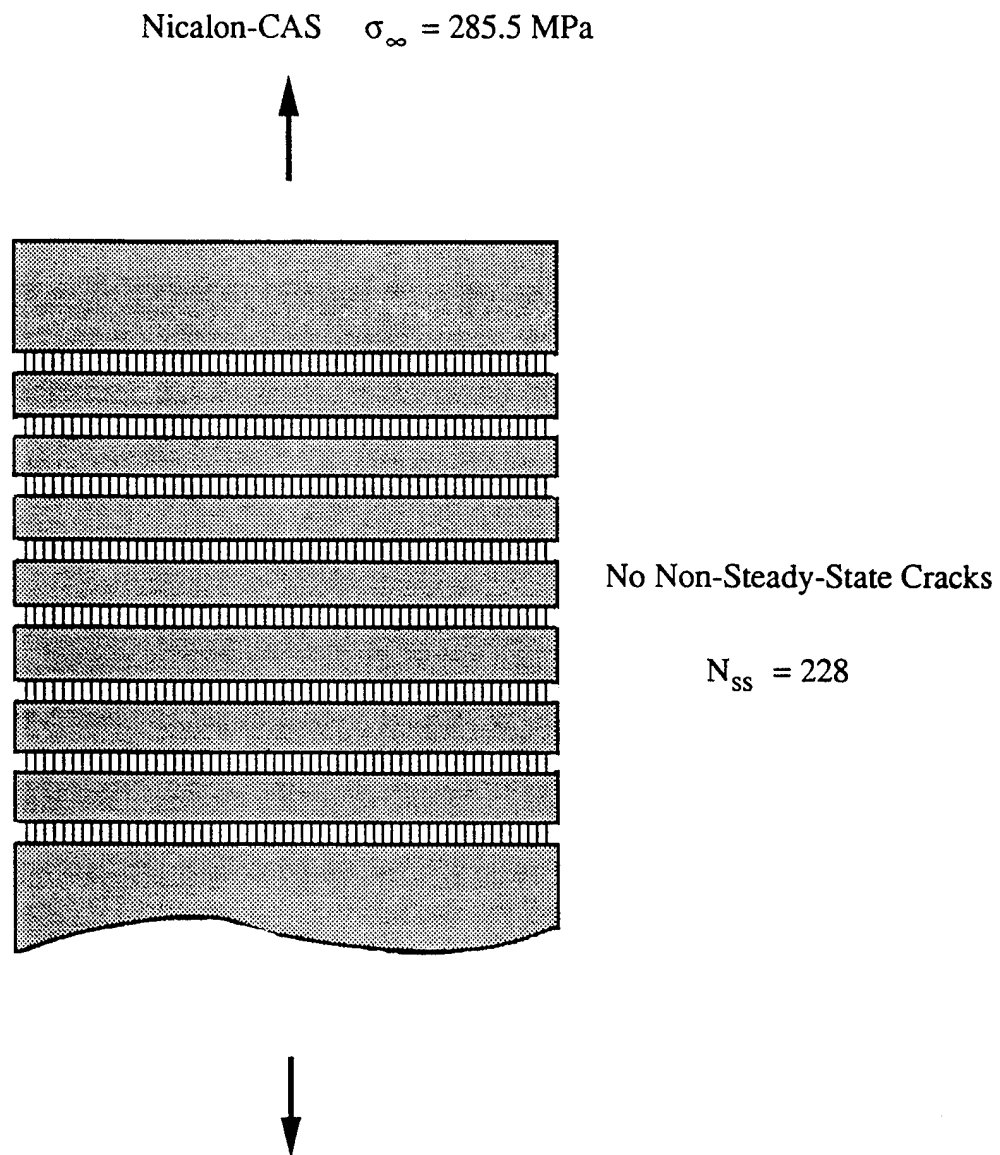


Figure 16 (f). Simulated Crack Evolution of Nicalon-CAS Composite - Continued.

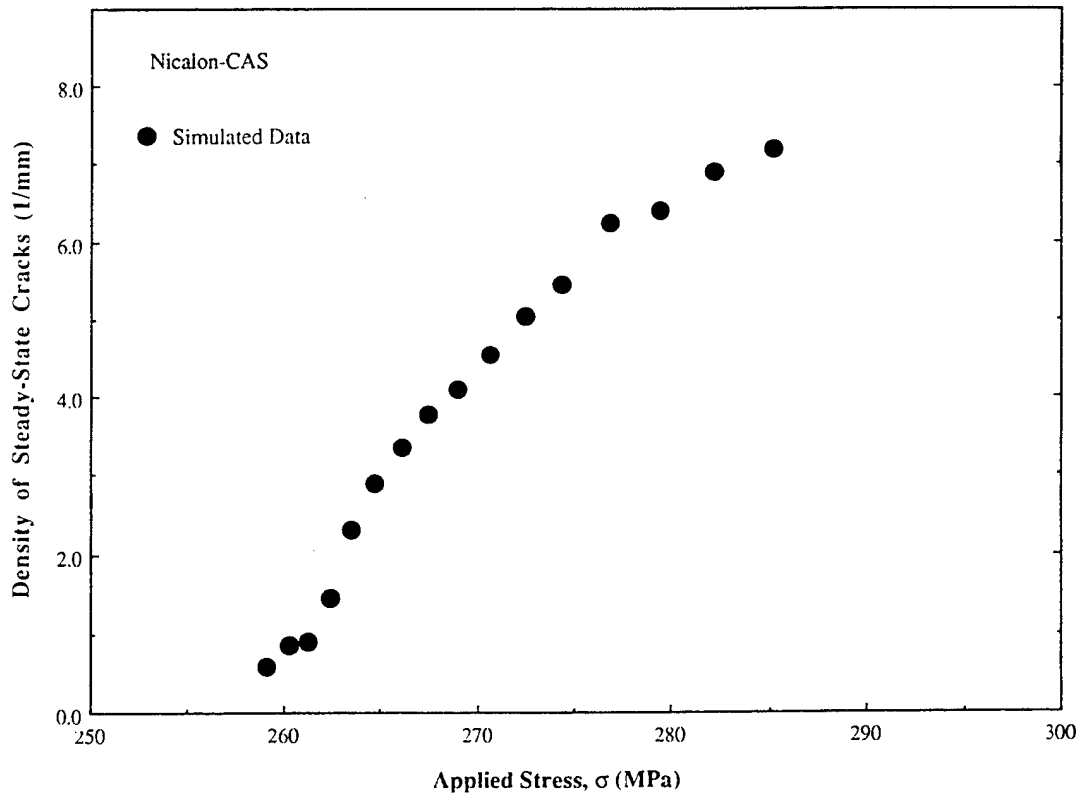


Figure 17. Steady-State Crack Density as a Function of the Applied Stress for the Nicalon-CAS Composite.

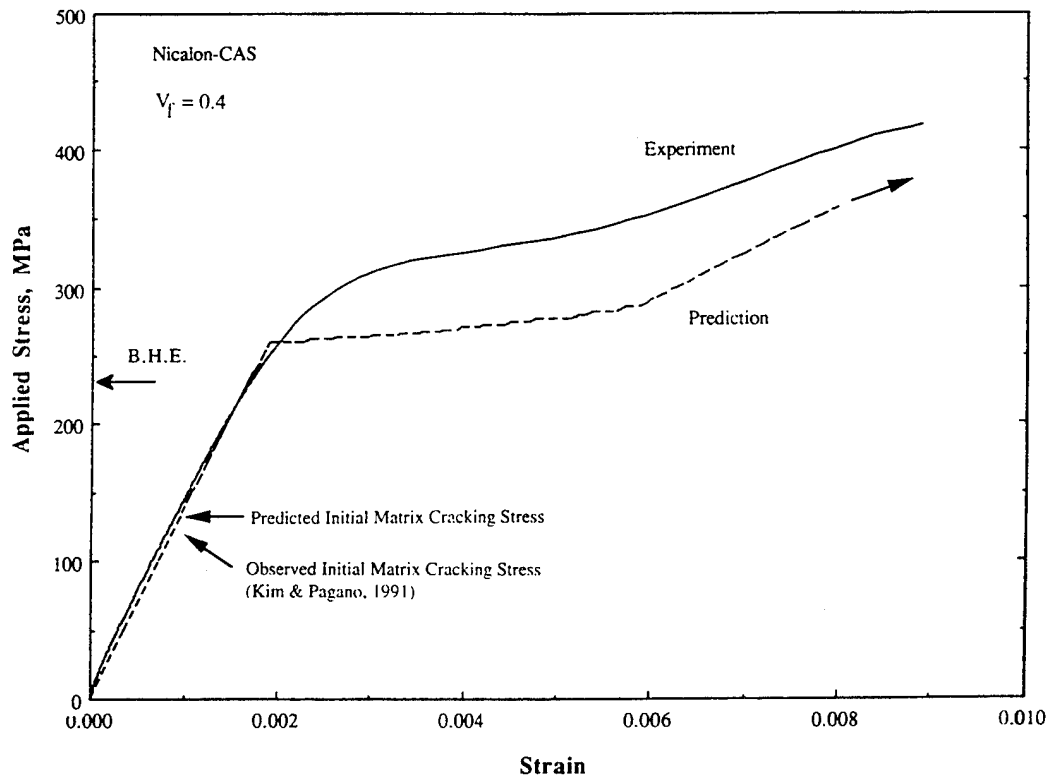


Figure 18. Comparison of the Predicted and the Measured Stress - Strain Relations of the Nicalon-CAS Composite.

Figures 19(A) and 19(B) show the matrix cracks on the failed gage section of the SiC-CAS composite specimen. Periodic matrix cracks were observed, however, the spacing of the cracks was not constant and some cracks appeared to be not straight cross-sectional cracks but were stopped or deviated by the fibers. Such interaction between cracks and fibers were not considered in the present model. In addition, fiber fracture, as shown in Fig 19(B), was observed in many places. This could produce more strain energy in the gage section during loading than the present model estimated.

*6.3.2 SiC-MAS Composite:* The simulated crack evolution of the SiC-MAS composite was similar to the one shown for the SiC-CAS composite. Therefore, it will not be illustrated again. In summary, a total of 281 planes were assigned to the gage section of the specimen, and 2137 FFZs were distributed on each plane. The larger number of planes in the gage section and smaller number of FFZs on each plane as compared to the SiC-CAS composite were due to the shorter sliding length ( $l$ ) and the smaller cross sectional area for the SiC-MAS specimen, respectively. Figure 20 shows the predicted average steady-state crack density as a function of the applied stress. The steady-state matrix cracking started at 607.5 MPa (cracks initiated from the 52.5  $\mu\text{m}$  FFZs) and completed at 619.3 MPa (cracks initiated from 42.5  $\mu\text{m}$  FFZs), after that, the stress-strain relation was governed by the completely cracked gage section with periodic matrix blocks.

Figure 21 shows the comparison of the predicted and the measured stress-strain relations. The model predicted an initial matrix cracking stress of 252.8 MPa. There is, however, no acoustic emission data available for comparison. Without incorporating fiber fractures, the model predicted a stress-strain relation similar to that of the SiC-CAS material with the exception of two important features: (1) the steady-state cracking regime occurred at much higher stresses. This could be mainly attributed to the compressive residual stress present in the matrix, the higher matrix fracture toughness, as well as the smaller FFZs sampled from the microstructure; (2) the total inelastic strain due to matrix cracking was smaller. This was mainly due to the smaller size range of the FFZs which controlled the steady-state cracking on all the planes. In other words, this could be attributed to the more uniform fiber distribution in the Nicalon-MAS composite. On the other hand, the experimentally measured  $\sigma - \epsilon$  relation indicated a more brittle type of behavior with a failure strain of only 0.4%. This was suspected to be due to the high interfacial sliding stress in this composite which enhanced the fracture of fibers and limited the ultimate strength. The initial elastic modulus was estimated to be  $\sim 160$  GPa, accordingly the proportional limit was at  $\sim 310$  MPa.

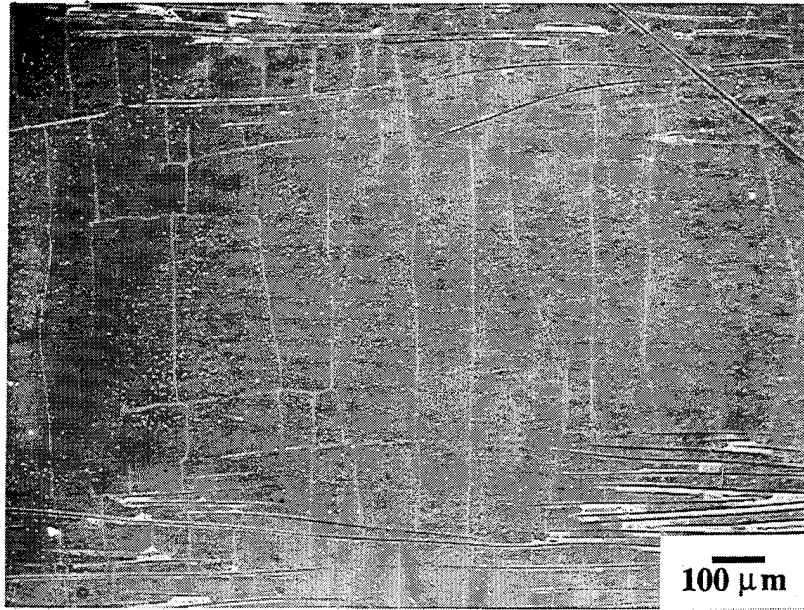


Figure 19(A). SEM Micrographs of the Matrix Cracks of Nicalon-CAS.

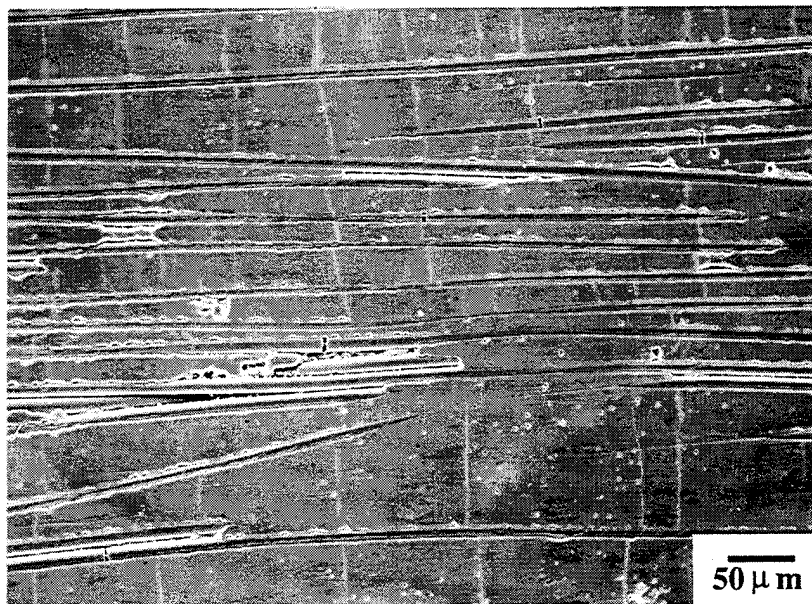


Figure 19(B). Fiber Fractures Observed at Higher Magnification (Nicalon-CAS)

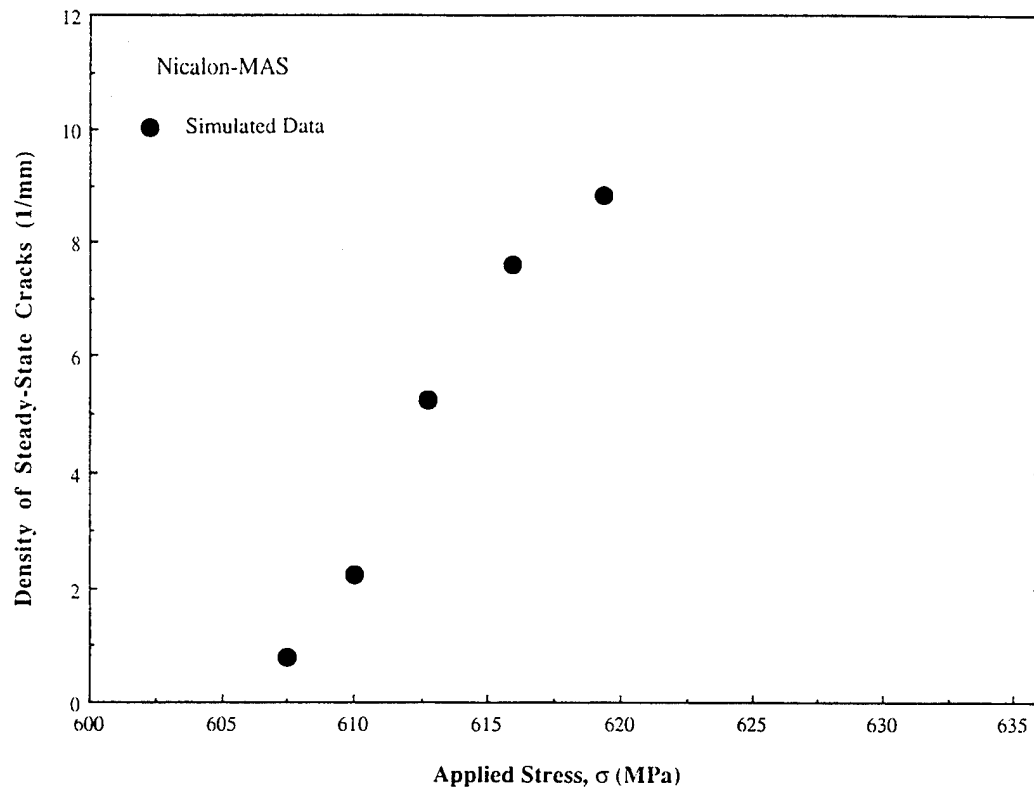


Figure 20. Average Steady-State Crack Density as a Function of the Applied Stress (Nicalon-MAS).

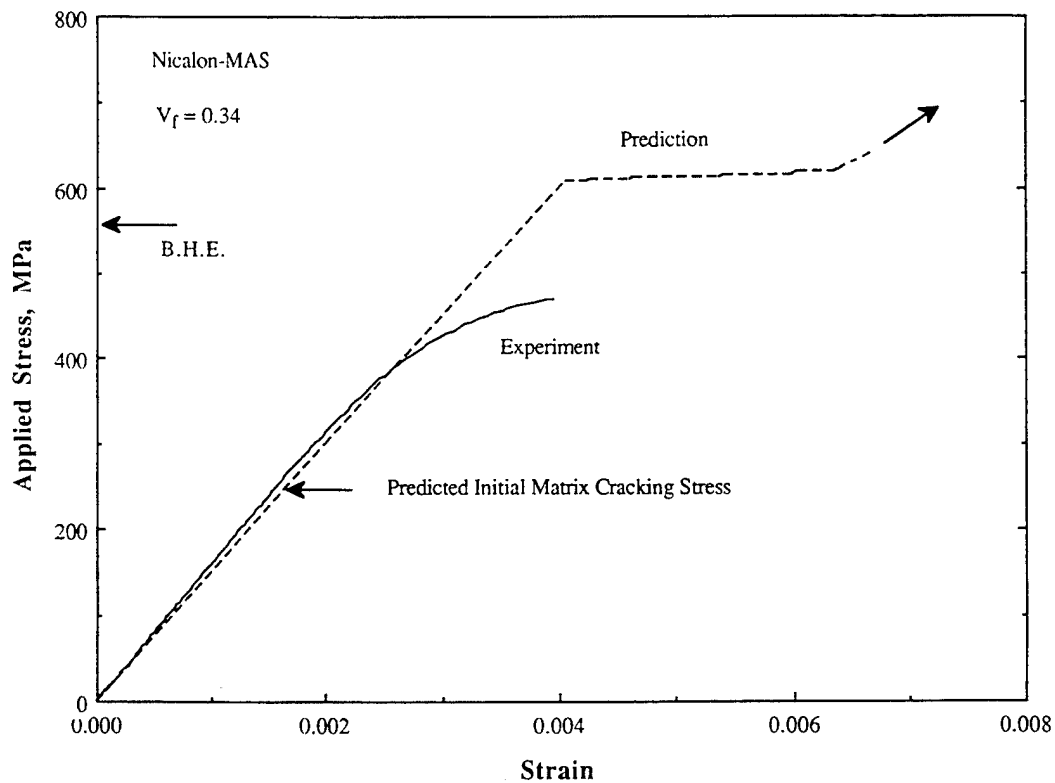


Figure 21. Comparison of the Predicted and the Measured Stress – Strain Relations (Nicalon-MAS).

Figure 22(A) shows a typical failed gage section of the SiC-MAS composite specimen. It was found that there were no periodic steady-state cracks in the gage section, but only local damage of the matrix in the form of short cracks in the vicinity of the failed section. Significant amount of fiber fractures were observed. Figure 22(B) shows a typical fracture surface of the Nicalon fiber. The fracture surface morphologies indicated that the fractures were initiated from surface flaws.

It is interesting to make a further correlation here between the failed gage section surface and the measured  $\sigma - \epsilon$  relation. Although the specimen examinations have indicated that the ultimate strength of this composite was limited by fiber fractures before steady-state cracks could be developed to provide significant inelastic strain, the measured stress - strain relation, however, showed pronounced inelastic behavior. In other words, the exhibited gradual transition from elastic toward inelastic regime, in the measured stress - strain curve, was mainly due to fibers fractures. This observation strongly suggests that the present model should take into account the progressive fiber fracture behavior to produce more gradual transition from the elastic to the inelastic tensile behaviors.

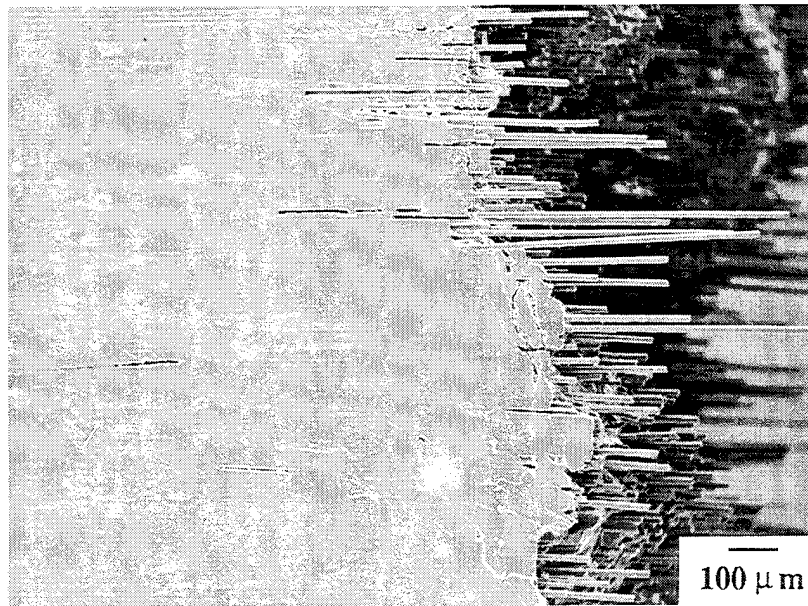


Figure 22(A). SEM Micrograph of the Failure Gage Section (Nicalon-MAS).



Figure 22(B). Typical Fracture Surface of the Nicalon-Fiber.



## 7. DISCUSSIONS

### 7.1 Effect of Variability of the Input Parameters on the Prediction

The input parameters of the model included the elastic moduli of the matrix and the fiber,  $E_m$  and  $E_f$ ; the Poisson's ratios of the matrix and the fiber,  $\nu_m$  and  $\nu_f$ ; fiber radius,  $R$ ; fiber volume fraction,  $V_f$ ; fracture toughness of the matrix,  $K_{cm}$ ; the interfacial sliding stress,  $\tau$ ; the axial residual stress in the matrix,  $\sigma_m^I$ ; and the FFZ size distribution. Among these parameters, the elastic properties of the constituents are well known, the fiber radius, fiber volume fraction, and the FFZ size distribution were accurately measured using quantitative image analysis. The remaining parameters ( $K_{cm}$ ,  $\tau$ ,  $\sigma_m^I$ ), on the other hand, had to be based on such independent tests as fracture toughness tests and fiber push-in or push-out tests. Different tests, however, usually result in slightly different values of these properties[20,21] and consequently result in different predictions. Effects of the variability of the material properties on the predicted stress-strain relation could be clearly seen by showing their influence on the cracking stress - crack size relations. In the following, calculation was performed using the SiC-CAS composite as an example.

*7.1.1 Fracture Toughness of the Matrix:* Figure 23 shows the sensitivity of cracking stress - crack size relation to the matrix fracture toughness. The calculation was performed using the largest cracks which were present in the composite because the initial matrix cracking stress was determined by such cracks. The intermediate toughness value shown on the figure was used to obtain the predicted  $\sigma - \epsilon$  curve. The other two values represent the highest and the lowest values which have been reported in the literature[20]. As can be seen, higher fracture toughness results in higher matrix cracking stress (including the initial cracking stress) of the same crack size. The arrow on the figure indicates the (identical) crack size at instability. The variation in the matrix cracking stress at instability due to varying fracture toughness is quite significant and it implies that increase in the matrix fracture toughness can significantly raise up the steady-state matrix cracking stresses of the composite.

*7.1.2 Interfacial Sliding Stress:* Figure 24 shows the influence of the interfacial sliding stress on the cracking stress - crack size relation. Calculation was also performed on the largest crack size present in the SiC-CAS composite. Except the initial matrix cracking stress, the subsequent stable and unstable matrix cracking stresses are higher for higher interfacial sliding stress. The intermediate  $\tau$  value was used to obtain the prediction of the  $\sigma - \epsilon$  curve while the other two values represented the highest and the lowest sliding

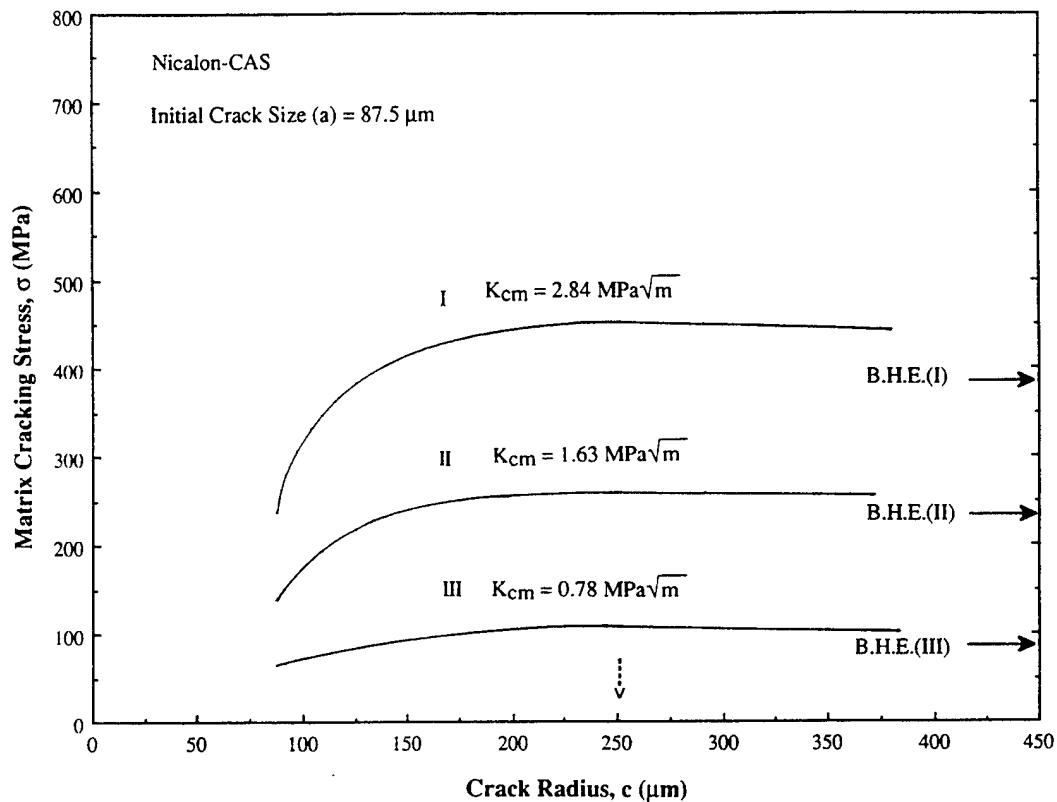


Figure 23. Effect of Matrix Fracture Toughness on the Cracking Stress – Crack Size Relation.

friction stresses reported in the literature[21]. The influence of the interfacial sliding friction stress on the matrix cracking stress was not as significant as the matrix fracture toughness. The identical initial matrix cracking stress predicted for the different sliding stresses reflects an intrinsic feature of the stress-intensity model. The difference between the two critical matrix cracking stresses predicted by the highest and the lowest sliding stresses was  $\sim 100$  MPa, a value smaller than the corresponding difference in Fig. 23. Nevertheless, it should be noted that the critical crack size defined by the cracking stress - crack size relation was different for different sliding stresses (as indicated by the arrows). Specifically, the critical crack size increased with increasing sliding stress. As a result, higher sliding stress would produce longer partially-bridged cracks and store more strain energy before steady-state cracking would occur. It should be emphasized that sliding stress also has influence on the fiber fracture and the ultimate strength of the composite[22]. Tailoring and optimization of the interfacial properties of a composite should consider its influence on the matrix cracking stress, fiber fracture and the anticipated application of the composite.

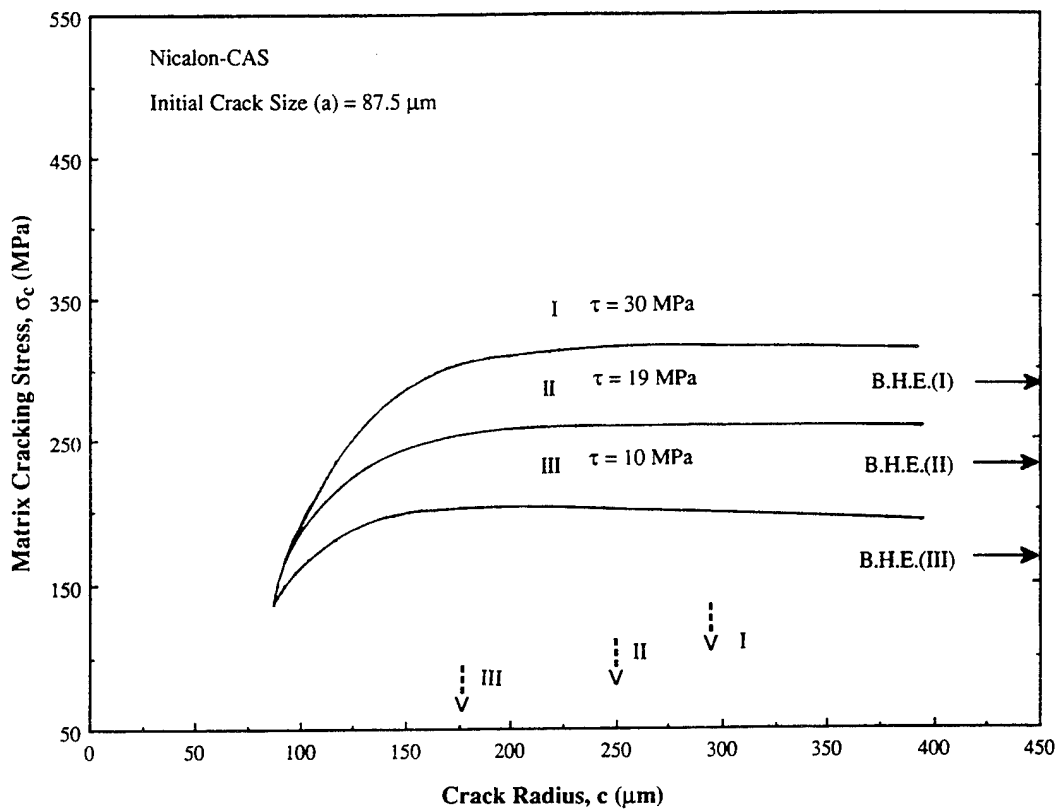


Figure 24. Influence of Interfacial Sliding Stress ( $\tau$ ) on the Cracking Stress – Crack Size Relation.

**7.1.3 Matrix Residual Stress:** Figure 25 shows the effect of residual stress on the matrix cracking stress - crack size relation. A higher tensile residual stress predicted lower matrix cracking stress. The intermediate residual stress indicated on the figure was used for predicting the stress - strain relation of the composite; the other two values represented the limiting values reported in the literature[20]. The critical matrix cracking stress predicted from the lowest residual stress was about 50 MPa higher than the one predicted from the highest residual stress. As can be seen in the figure, the critical crack size also varied with matrix residual stress. With decreasing tensile residual stress, the critical crack size became larger and thus delayed the occurrence of steady-state matrix cracking. This analysis would suggest that a lower tensile residual stress (or compressive residual stress) would be preferred for a composite since it provides higher steady-state matrix cracking stresses. However, steady-state matrix cracking at appropriate timing (before the ultimate strength of the composite) is also necessary since it provides the basic toughening mechanism of the composite. Design of a composite should seek the balance between the required inelastic toughening behavior and the ultimate strength of the composite.

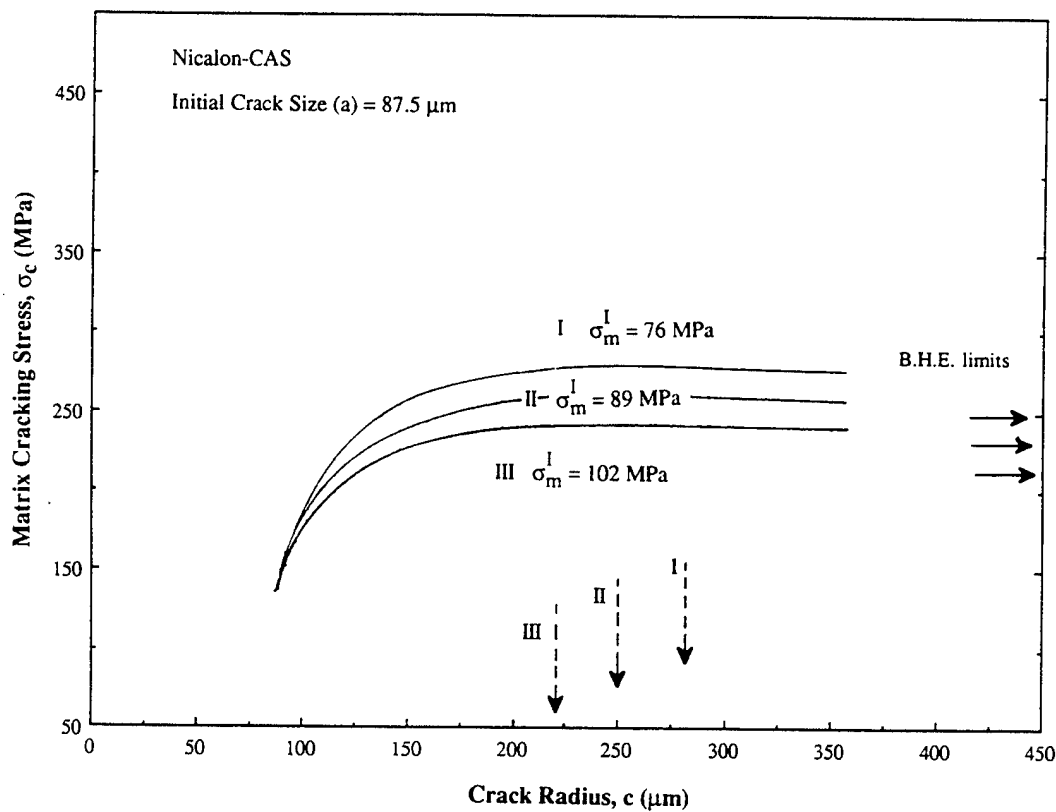


Figure 25. Effect of Matrix Residual Stress on the Cracking Stress – Crack Size Relation.

## 7.2 Directions to Improve the Predictive Capability of the Model

The present Phase I research was aimed at demonstrating the feasibility of combining the micromechanics treatment of a partially-bridged crack and the non-uniform fiber distribution nature of the composite to model the progressive damage and failure of fiber-reinforced ceramic matrix composites. Initial effort focused on the modeling of unidirectional composites. Two composites were selected for investigation. For the SiC-CAS composite, the present model gave good predictions of the initial matrix cracking stress and the total inelastic strain due to matrix cracking. For the SiC-MAS composite, the present model predicted much larger inelastic strain than what was observed experimentally. Experimental observations indicated the gradual transition from elastic to inelastic regimes on the stress-strain relation was due to fiber fractures. Therefore, incorporation of progressive fiber fracture in the present model is an important direction to improve the current model.

In addition, the model should also consider interaction between the matrix cracks on the same plane and interaction between cracks on the adjacent planes. Solutions

for the stress intensities of such interacting penny-shaped cracks are available in the literature[23] and can be incorporated in the model.

Furthermore, the methodology established in this research can be extended to model the stress - strain behavior of two-dimensional cross-ply laminated composites. For example, in the 0/90 laminated composites, the initial matrix damage is expected to occur in the laminates where the fibers are perpendicular to the loading direction ( $90^\circ$ ), followed by the matrix damage in the  $0^\circ$  laminates. Such two-stage damage process can be modeled using the same methodology outlined in this report.

### 7.3 What Will Happen If There Are No FFZs ?

The progressive damage model established in this research is based on the non-uniform fiber distribution found in typical commercial-grade fiber-reinforced ceramic composites. However, an interesting and hypothetical question is: if these composites can be manufactured with perfectly uniform fiber distribution, what does the present model predict? To answer this question, we should first review the damage process in the SiC-CAS composite: the initial matrix cracking occurred when the largest FFZs ( $a = 87.5 \mu\text{m}$ ) transformed to cracks. Steady-state matrix cracking started when these cracks extended unstably and completed when those cracks initiated from the  $50 \mu\text{m}$  FFZs became unstable. The cracks initiated from those FFZs less than  $50 \mu\text{m}$  does not have significant influence on the stress-strain behavior. As a result, the largest FFZs determine the two important stresses of the prediction: the initial matrix cracking stress and the onset of steady-state matrix cracking. With the same fiber volume fraction, if the composite has uniform fiber distribution the FFZ size distribution will become a delta function located at the average fiber spacing. Using the SiC-CAS composite as an example, the initial matrix cracking stress and the steady-state matrix cracking stress will be raised to 404.7 MPa and 530.3 MPa, respectively. The much higher load carrying capability due to uniform fiber distribution is quite attractive for this composite.

## 8. CONCLUSIONS

1. A computational model was developed to simulate the matrix-crack evolution and predict the stress-strain relation of unidirectional fiber-reinforced brittle matrix composites under uniaxial tensile loading. This model combined a micromechanics treatment of a partially-bridged crack and a size distribution of the fiber-free zones that served as an input for the initiation of small penny-shaped cracks in the early stage of loading.
2. Theoretically simulated stress - strain relation for the SiC-CAS composite achieved good agreement with the measured relation in both the initial matrix cracking stress and the total inelastic strain due to matrix cracking.
3. Measured stress - strain relation and the specimen examination of the SiC-MAS composite indicated that the ultimate strength and the amount of inelastic strain due to matrix cracking were limited by early fiber fracture. Pronounced gradual transition from elastic to inelastic stress-strain relation due to fiber fracture suggested that incorporation of the progressive fiber fracture in the model was important.

## 9. ACKNOWLEDGEMENT

The authors are grateful to

Drs. K. Chyung and D. Larsen of Corning Inc. for supplying the matrix materials for fracture toughness evaluation and helpful discussion on the materials properties.

Dr. P. R. King and his research assistants (Mr. S. Middlemiss and Mr. C. Schneider) of University of Utah, for assistance and helpful discussion on the application of Image Analyzer.

Dr. J. W. Holmes of University of Michigan for guidance and helpful discussion on the edge-loading tensile tests.

## 10. REFERENCES

1. Fiber Reinforced Ceramic Composites : Materials, Processing and Technology, K. S. Mazdiasni (Ed.), Noyes Publications (1990).
2. A. G. Evans and D. B. Marshall, " Mechanical Behavior of Ceramic-Matrix Composites "; pp.1-38 in Fiber Reinforced Ceramic Composites : Materials, Processing and Technology, K. S. Mazdiasni (Ed.), Noyes Publications (1990).
3. J. Aveston, G. A. Cooper and A. Kelly, " Single and Multiple Fracture "; pp.15-26 in The Properties of Fiber Composites, IPC Science and Technology Press (1971).
4. B. Budiansky, J. W. Hutchinson and A. G. Evans, " Matrix Fracture in Fiber-Reinforced Ceramics ", *J. Mech. Phys. Solids*, **34** [2] 167-89 (1986).
5. D. B. Marshall, B. N. Cox, and A. G. Evans, "The Mechanics of Matrix Cracking in Brittle-Matrix Fiber Composites," *Acta metall.*, **33** [11] 2013-21 (1985).
6. L. N. McCartney, "Mechanics of Matrix Cracking in Brittle-Matrix Fiber-Reinforced Composites," *Proc. R. Soc. Lond. A.*, **409**, 329-50 (1987).
7. B. S. Majumdar, G. M. Newaz, and A. R. Rosenfield, "Yielding Behavior of Ceramic Matrix Composites"; pp. 2805-14 in *Advances in Fracture Research*, Proc. of 7th International Conference on Fracture (ICF7). Edited by K. Salama, K. Ravi Chandar, D. M. R. Taplin, and P. Rama Rao, Pergamon Press (1989).
8. S. Danchaivijit and D. K. Shetty, "Matrix Cracking in Ceramic-Matrix Composites ",*J. Am. Ceram. Soc.*, **76** [10] 2497-504 (1993).
9. R. Y. Kim and N. J. Pagano, " Crack Initiation in Unidirectional Brittle-Matrix Composites ", *J. Am. Ceram. Soc.*, **74** [5] 1082-90 (1991).
10. D. K. Shetty, " Overview of Design Methodology for Ceramic-Matrix Composites "; Chapter 13 in *Handbook on Continuous Fiber Reinforced Ceramic-Matrix Composites*, In Press (1995).
11. A. G. Evans, " Perspective on the Development of High-Toughness Ceramics," *J. Am. Ceram. Soc.*, **73** [2] 187-206 (1990).
12. S. Danchaivijit, D. K. Shetty, and J. Eldridge, " Critical Stresses for Extension of Filament-Bridged Matrix Cracks in Ceramic-Matrix Composites: An Assessment with a Model Composite with Tailored Interfaces," *J. Am. Ceram. Soc.*, in press.
13. I. N. Sneddon and M. Lowengrub, *Crack Problems in the Classical Theory of Elasticity*, John Wiley & Sons, Inc. (1969).
14. R. P. King and C. L. Schneider, " An Effective SEM-Based Image Analysis System for Quantitative Mineralogy," *KONA*, **11**, pp. 165 (1993).



15. F. W. Zok and S. M. Spearing, " Matrix Crack Spacing in Brittle Matrix Composites," *Acta. metall. mater.* **40** [8] 2033-43 (1992).
16. W. H. Press, B. P. Flannery, S. A. Teukolsky, and W. T. Vetterling, " Chapter 7 Random Numbers," Numerical Recipes in C, Cambridge University Press, New York, (1990).
17. B. F. Sørensen and R. Talreja, " Effects of Nonuniformity of Fiber Distribution on Thermally-Induced Residual Stresses and Cracking in Ceramic Matrix Composites," *Mechanics of Materials*, **16**, pp 351-63 (1993).
18. J. W. Holmes, " A Technique for Tensile Fatigue and Creep Testing of Fiber-Reinforced Ceramics," *J. of Composite Materials*, **26** [6] 916-33 (1992).
19. Private conversation with Dr. John. W. Holmes, Composite Testing and Analysis, Ann Arbor, MI.
20. D.S. Beyerle, S. M. Spearing, F. W. Zok, and A. G. Evans, " Damage and Failure in Unidirectional Ceramic Matrix Composites," *J. Am. Ceram. Soc.*, **75** [10] 2719-25 (1992).
21. T. J. Mackin and F. W. Zok, " Fiber Bundle Pushout: A Technique for the Measurement of Interfacial Sliding Properties," *J. Am. Ceram. Soc.*, **75** [11] 3169-71 (1992).
22. M. D. Thouless, O. Sbaizero, L. S. Sigl, and A. G. Evans, " Effect of Interface Mechanical properties on Pullout in a SiC-Fiber-Reinforced Lithium Alumium Silicate Glass-Ceramic," *J. Am. Ceram. Soc.*, **72** [4] 525-532 (1989).
23. Stress Intensity Factors Handbook, Y. Murakami Edited. Pergamon Press, New York (1987).